

Nonlinear scattering based imaging in elastic media: Theory, theorems, and imaging conditions

Matteo Ravasi¹ and Andrew Curtis¹

ABSTRACT

With the more widespread introduction of multicomponent recording devices in land and marine ocean-bottom seismic acquisition, elastic imaging may become mainstream in coming years. We have derived new, nonlinear, elastic imaging conditions. A correlation-type representation theorem for perturbed elastic media, commonly used in seismic interferometry to explain how a scattered wave response between two receivers/sources may be predicted given a boundary of sources/receivers, can be considered as a starting point for the derivation. Here, we use this theorem to derive and interpret imaging conditions for elastic migration by wavefield extrapolation (e.g., elastic reverse-time migration). Some approximations lead to a known, heuristically derived imaging condition that crosscorrelates

P- and S-wave potentials that are separated in the subsurface after full-wavefield extrapolation. This formal connection reveals that the nonapproximated correlation-type representation theorem can be interpreted as a nonlinear imaging condition, that accounts also for multiply scattered and multiply converted waves, properly focusing such energy at each image point. We present a synthetic data example using either an ideal (acquisition on a full, closed boundary) or a real (partial boundary) seismic exploration survey, and we demonstrate the importance of nonlinearities in pure- and converted-mode imaging. In PP imaging, they result in better illumination and artifact reduction, whereas in PS imaging they show how zero time-lag and zero space-lag crosscorrelation imaging conditions are not ideal for imaging of converted-mode waves because no conversion arises from zero-offset experiments.

INTRODUCTION

Seismic imaging is the process through which seismic data recorded on the earth's surface are mapped into the subsurface to create a spatial image of some property of the earth. In other words, an inverse scattering problem is solved to undo all of the wave-propagation effects (e.g., refractions, reflections, diffractions) occurring from the time a source is fired to the time a receiver records the earth's response. In the literature, two classes of techniques are distinguished (Wapenaar, 1996): inversion and migration. Inversion of elastic earth response data, often used in the form of full- or partitioned-waveform inversion (henceforth, FWI) was introduced by Tarantola (1986) with good examples in Mora (1987), Sears et al. (2008), and Brossier et al. (2009). In principle, recorded waveforms are inverted fully nonlinearly for a model of earth

parameters that predicts the recorded data. By contrast, the earliest forms of migration involved moving (migrating) energy around seismic time sections to estimate the true subsurface position of spatial changes of the medium parameters (the reflectivity) — see Yilmaz (1989). For this reason, the word “migration” is often used as synonymous with “imaging,” particularly in an exploration context. Migration is commonly based on a linearized, single-scattering approximation called the Born approximation (Oristaglio, 1989). Only energy from primary reflections or diffractions is therefore properly focused by migration; multiples and higher-order scattering events must generally be attenuated at an early stage of data processing to prevent the distortion of seismic images.

Nowadays, a more sophisticated view of migration is emerging with the aim to produce (so-called) “true-amplitude images” (images where reflectivity estimates are directly related to the values

Manuscript received by the Editor 24 July 2012; revised manuscript received 10 November 2012; published online 29 April 2013.

¹The University of Edinburgh, School of GeoSciences, Grant Institute, Kings Buildings, Edinburgh, UK. E-mail: M.Ravasi@sms.ed.ac.uk; andrew.curtis@ed.ac.uk.

© 2013 Society of Exploration Geophysicists. All rights reserved.

of elastic rock-physics parameters) of complex geologic regions. This is desirable because careful syntheses of reflection amplitudes are crucial for amplitude-versus-offset (AVO) analysis to be robust. Reverse-time migration (RTM) is one promising tool to achieve this goal because it is a migration technique based on the full wave equation, in principle requiring no single-scattering approximation. Historically, RTM is based on the concept of so-called adjoint-state methods (Plessix, 2006); it can also be seen as a single iteration in the optimization of a FWI objective function (see Tromp et al., 2005).

The RTM algorithm consists of two consecutive steps: First, the incident wavefield is modeled synthetically using a source at any physical source location (the source wavefield), and the scattered wavefield is extrapolated by synthetic backward propagation in time of the data recorded at the surface (the receiver wavefield). This is followed by the application of an imaging condition (IC) (Claerbout, 1971) — an equation which combines source and receiver wavefields at each point in the medium to construct an estimate of the subsurface structure (the so-called “seismic image”).

Recently, an explicit link has been established between seismic interferometry and reverse-time imaging in acoustic media (Curtis, 2009; Curtis and Halliday, 2010; Halliday and Curtis, 2010). This has allowed the wavefield-extrapolation step and various imaging conditions to be reinterpreted in terms of physical wave-propagation phenomena, and to be reformulated in a nonlinear fashion using representation theorems (Vasconcelos et al., 2009a, 2010, 2012; Halliday and Curtis, 2010; Sava and Vasconcelos, 2011; Vasconcelos, 2011; Fleury and Vasconcelos, 2012). In this paper, we focus our attention on elastic migration by wavefield extrapolation (for example, by elastic RTM), and we use a correlation-type representation theorem in elastic media to identify a new set of true-amplitude, nonlinear ICs.

Seismic interferometry usually refers to the synthesis of the wavefield that would propagate between two receiver locations, as if one receiver was replaced by a source (Figure 1a). This is obtained by crosscorrelating the wavefields observed at each receiver location due to an enclosing boundary of energy sources (Wapenaar, 2004; van Manen et al., 2005, 2006; Wapenaar and Fokkema, 2006). Introductions, tutorials, and reviews are given in Curtis et al. (2006), Wapenaar et al. (2010a, 2010b), and Galetti and Curtis (2012). Slob et al. (2007) showed that crossconvolution can also be used to construct interreceiver wavefields (in the geometry of Figure 1b), and Vasconcelos and Snieder (2008a, 2008b)

first used deconvolution to perform interferometry. By reciprocity it was shown that the Green’s function between two sources can also be estimated given their recordings on a boundary of receivers (as in Figure 1c; also Hong and Menke, 2006; Curtis et al., 2009). Finally, if we have a boundary of sources and a boundary of receivers, Curtis (2009), Curtis and Halliday (2010), Halliday and Curtis (2010) and Curtis et al. (2012) demonstrated that the Green’s function between a physical source and physical receiver that are not on either boundary can be constructed using appropriate crosscorrelation and/or crossconvolution operations (Figure 1d). The latter method is referred to as “source-receiver interferometry.”

It is also important that Vasconcelos et al. (2009a) and Sava and Vasconcelos (2011) found a connection between the zero time-lag and zero space-lag crosscorrelation imaging condition invoked by most wave-equation-based imaging methods (e.g., Claerbout, 1985), and the theory and practice of seismic interreceiver interferometry. Halliday and Curtis (2010) use the theory of source-receiver interferometry to generalize that connection by deriving a new form of integral that describes the recovery of scattered waves propagating between a real source and a real receiver. They include terms that describe the propagation of wavefields from a boundary of sources to any image point, and to a boundary of receivers from the image point. Thus, they were able to create an explicit analytic link between this form of seismic interferometry and inverse-scattering seismic imaging theory: By using a single-scattering Born approximation, they present an alternative derivation of Oristaglio’s inverse-scattering formula (Oristaglio, 1989) which is equivalent to many currently used migration algorithms, and which they derive directly from source-receiver interferometry. By removing the Born approximation, they obtain a nonlinear imaging theorem that accounts for multiple scattering, and the correct distribution of energy in the scattered waves as is described by the optical theorem of physics (Snieder et al., 2008; Halliday and Curtis, 2009).

In the context of interreceiver interferometry, Fleury and Vasconcelos (2012) define for the first time a nonlinear imaging condition that may be suitable for practical applications, which takes into account amplitude corrections necessary to migrate multiply scattered waves (e.g., reflection multiples). This imaging condition was shown to produce an image that is approximately the zero-time, scattered-wave response generated by zero-offset pseudoexperiments between a source and a receiver located exactly at each and every image point. Building on the new form of source-receiver

interferometry for scattered wavefields of Halliday and Curtis (2010), Vasconcelos (2011) and Vasconcelos et al. (2012) define a nonlinear source-receiver imaging framework, where the imaging condition and the wavefield extrapolation make proper use of vector-acoustic fields and higher-order scattering events rather than only primary events. In this paper, we extend this body of work to elastic wavefields.

Over recent decades, acquisition technologies have improved with the introduction of multi-component recording devices for land, ocean-bottom, and marine seismic surveys. They record not only the vertical component of particle displacement (or particle velocity) but also the horizontal components. New geophysical techniques have been developed to take advantage of

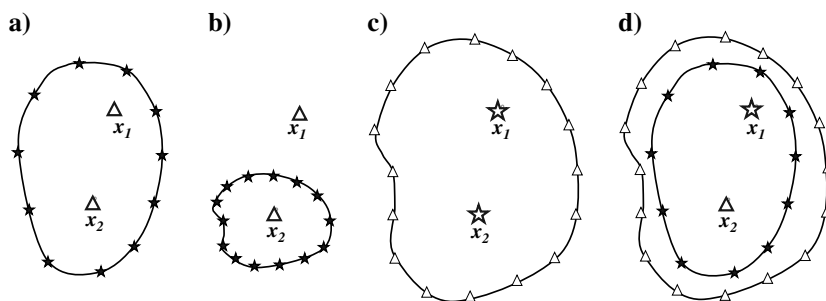


Figure 1. Configurations for (a) interreceiver correlational interferometry, (b) interreceiver convolutional interferometry, (c) intersource correlational interferometry, and (d) source-receiver interferometry using two correlational integrals. Stars and triangles indicate sources and receivers on the boundaries. Interferometry is used to construct the wavefield between the open stars and the open triangles.

these acquisition developments, especially in data processing such as noise attenuation, signal reconstruction, and interpolation or multiple attenuation. On the other hand, even though multicomponent imaging has been an active research area for many years, multicomponent data are not usually processed with specifically designed imaging techniques.

For isotropic media, the most straightforward way to process these data is based on the assumption that P- and S-waves can be separated on the recording surface from multicomponent data, and each can be imaged independently with procedures borrowed from acoustic wave equation imaging algorithms, using P- and S-wave velocities, respectively. Early attempts at multicomponent imaging used the Kirchhoff integral and separated waves on the earth's free surface involved computing traveltimes for PP and PS reflections and summing data along those trajectories (e.g., Wapenaar and Haimé, 1990). Yan and Sava (2008) suggest an alternative procedure that employs the entire vector wavefield for wavefield reconstruction, then separates P- and S-waves after extrapolating the full vector wavefield into the subsurface, just before the imaging condition is applied. They also formulate a new set of imaging conditions that combine the various incident and reflected wave modes.

The recently increasing interest in recording multicomponent wavefields, and in seismic scattering and imaging based on the elastic wave equation, indicates that the interferometric nonlinear imaging conditions proposed so far in the acoustic case could usefully be extended to the elastic case. Here, we first consider the correlation-type representation theorem in elastic media (van Manen et al., 2006; Wapenaar and Fokkema, 2006) and explicitly express the construction of only the scattered wavefield. We manipulate this formula to obtain a new set of imaging conditions that crosscorrelate P- and S-wave potentials separated in the subsurface after a full-wavefield extrapolation. These are suitable for use with land and marine ocean-bottom seismic acquisition. We then show how one can approximate and linearize our expressions to obtain an imaging condition that is identical to that proposed by Yan and Sava (2008). This suggests that, without these approximations, the correlation-type representation theorem can be regarded as a nonlinear, true-amplitude version of the latter imaging condition, that accounts also for multiply scattered and converted waves.

We demonstrate this with a synthetic example, in which two different acquisition geometries are used. First, a full boundary of sources allows for a perfect construction of the scattered-wave Green's function at each and every image point: its zero-time value is the elastic image. Then the effect of more practical source coverage and partial illumination is investigated by using only a portion of the source boundary for the image construction. These examples highlight many interesting issues; for instance, how partial illumination affects nonlinear imaging, and why there is debate about how to choose signs in PS-wave imaging conditions (see the Discussion section). In fact, we show that PS imaging is only possible using previous zero-offset ICs because of the incompleteness of the source boundary, and hence works only because the full theory breaks down.

REPRESENTATION THEOREM FOR PERTURBED ELASTIC MEDIA

Given an elastic lossless medium, our starting point for the derivation of reciprocity and representation theorems is the wave equation for the displacement vector in the frequency domain. Using the Fourier convention $f(t) = (1/2\pi) \int F(\omega) e^{-j\omega t} d\omega$, the wave equation is

$$\rho(\mathbf{x})\omega^2 u_i(\mathbf{x}, \omega) + \partial_j(c_{ijkl}(\mathbf{x})\partial_k u_l(\mathbf{x}, \omega)) = -f_i(\mathbf{x}, \omega), \quad (1)$$

where $u_i(\mathbf{x}, \omega)$ is the i th component of the particle displacement vector, $f_i(\mathbf{x}, \omega)$ is the i th component of the body-force density, ∂_j is the spatial partial derivative with respect to the x_j coordinate ($\partial_j g = \frac{\partial g}{\partial x_j}$), $c_{ijkl}(\mathbf{x})$ is the elasticity tensor or stiffness, and $\rho(\mathbf{x})$ is the density. Note that Einstein's summation convention for repeated indices is used throughout this paper. To proceed, it is convenient to define a compact notation for this wave equation

$$W_i = \rho\omega^2 u_i + \partial_j(c_{ijkl}\partial_k u_l) + f_i = 0, \quad (2)$$

where we have dropped the explicit notation of spatial and frequency dependence of the various terms (which is nevertheless implicitly assumed).

Given two different waves states A and B , where a "state" means a "combination of medium parameters, field quantities, source quantities, boundary conditions, and initial conditions that satisfy the wave equation," a Betti-Rayleigh reciprocity theorem of the correlation-type can be derived by multiplying the complex conjugate wave equation for state B by u_i^A and the wave equation for state A by u_i^{B*} , and subtracting the results

$$u_i^A W_i^{B*} - u_i^{B*} W_i^A = 0, \quad (3)$$

where W_i^A is the wave state in case A , and similarly for state B . Integrating over a volume V with closed boundary ∂V , and using Gauss' theorem to convert volume integrals into surface integrals (Aki and Richards, 1980; Snieder, 2002) we obtain

$$\begin{aligned} & \int_{\partial V} \{u_i^{B*} n_j c_{ijkl} \partial_k u_l^A - u_i^A n_j c_{ijkl} \partial_k u_l^{B*}\} dx^2 \\ & = \int_V \{u_i^A f_i^{B*} - u_i^{B*} f_i^A\} dx^3, \end{aligned} \quad (4)$$

where we have accounted for the symmetry properties of the elasticity tensor ($c_{ijkl} = c_{klij}$) to derive equation 4 from equation 3. Note that n_j is the j th component of the outward normal vector to the boundary ∂V .

If we now introduce the Green's function for states A and B by taking \mathbf{f}^A as an impulsive point source of force at location \mathbf{x}_A in the fixed m th direction ($f_i^A = \delta_{im} \delta(\mathbf{x} - \mathbf{x}_A)$) and \mathbf{f}^B as a source of the same type at location \mathbf{x}_B in the fixed m th direction ($f_i^B = \delta_{im} \delta(\mathbf{x} - \mathbf{x}_B)$), the general field quantities $\mathbf{u}^A(\mathbf{x})$ and $\mathbf{u}^B(\mathbf{x})$ turn into specific Green's functions (by definition)

$$u_i^A(\mathbf{x}) = G_{in}(\mathbf{x}, \mathbf{x}_A) \quad u_i^B(\mathbf{x}) = G_{im}(\mathbf{x}, \mathbf{x}_B). \quad (5)$$

Substituting into equation 4, assuming \mathbf{x}_A and \mathbf{x}_B are situated in V , and using source-receiver reciprocity gives

$$\begin{aligned} G_{in}(\mathbf{x}_B, \mathbf{x}_A) - G_{in}^*(\mathbf{x}_B, \mathbf{x}_A) &= \int_{\partial V} \{G_{im}^*(\mathbf{x}_B, \mathbf{x}) n_j c_{mjkl} \partial_k G_{ni}(\mathbf{x}_A, \mathbf{x}) \\ & - G_{nm}(\mathbf{x}_A, \mathbf{x}) n_j c_{mjkl} \partial_k G_{il}^*(\mathbf{x}_B, \mathbf{x})\} dx^2. \end{aligned} \quad (6)$$

This is the correlation-type representation theorem for elastic media (Van Manen et al., 2006). This equation shows that the difference of the Green's function and its complex conjugate (so-called homogeneous Green's function) can be computed (represented) between two points \mathbf{x}_A and \mathbf{x}_B everywhere inside the volume V if responses

to force and deformation sources between the enclosing boundary ∂V and each of these points are known.

The propagation domain can be considered to be composed of an unperturbed medium with elasticity tensor $c_{ijkl}^0(\mathbf{x})$ and density $\rho^0(\mathbf{x})$, and a perturbation defined by $c_{ijkl}^S(\mathbf{x}) = c_{ijkl}(\mathbf{x}) - c_{ijkl}^0(\mathbf{x})$, and $\rho^S(\mathbf{x}) = \rho(\mathbf{x}) - \rho^0(\mathbf{x})$. We write for the Green's functions

$$G(\mathbf{x}_A, \mathbf{x}) = G^0(\mathbf{x}_A, \mathbf{x}) + G^S(\mathbf{x}_A, \mathbf{x}), \quad (7)$$

and similarly for state B , where the superscript 0 indicates the wavefield in the reference medium and superscript S indicates the wavefield perturbation caused by medium changes, the latter usually being referred to as the scattered component of the wavefield (Figure 2). Substituting equation 7 and similar expressions for the other Green's functions into the right-hand side (RHS) of equation 6 gives

$$\begin{aligned} & G_{in}(\mathbf{x}_B, \mathbf{x}_A) - G_{in}^*(\mathbf{x}_B, \mathbf{x}_A) \\ &= \int_{\partial V} \{G_{im}^{0*}(\mathbf{x}_B, \mathbf{x}) n_j c_{mjkl} \partial_k G_{nl}^0(\mathbf{x}_A, \mathbf{x}) \\ &\quad - G_{nm}^0(\mathbf{x}_A, \mathbf{x}) n_j c_{mjkl} \partial_k G_{il}^{0*}(\mathbf{x}_B, \mathbf{x})\} dx^2 \leftarrow I_{00} \\ &\quad + \int_{\partial V} \{G_{im}^{0*}(\mathbf{x}_B, \mathbf{x}) n_j c_{mjkl} \partial_k G_{nl}^S(\mathbf{x}_A, \mathbf{x}) \\ &\quad - G_{nm}^S(\mathbf{x}_A, \mathbf{x}) n_j c_{mjkl} \partial_k G_{il}^{0*}(\mathbf{x}_B, \mathbf{x})\} dx^2 \leftarrow I_{0S} \\ &\quad + \int_{\partial V} \{G_{im}^{S*}(\mathbf{x}_B, \mathbf{x}) n_j c_{mjkl} \partial_k G_{nl}^0(\mathbf{x}_A, \mathbf{x}) \\ &\quad - G_{nm}^0(\mathbf{x}_A, \mathbf{x}) n_j c_{mjkl} \partial_k G_{il}^{S*}(\mathbf{x}_B, \mathbf{x})\} dx^2 \leftarrow I_{S0} \\ &\quad + \int_{\partial V} \{G_{im}^{S*}(\mathbf{x}_B, \mathbf{x}) n_j c_{mjkl} \partial_k G_{nl}^S(\mathbf{x}_A, \mathbf{x}) \\ &\quad - G_{nm}^S(\mathbf{x}_A, \mathbf{x}) n_j c_{mjkl} \partial_k G_{il}^{S*}(\mathbf{x}_B, \mathbf{x})\} dx^2 \leftarrow I_{SS}, \quad (8) \end{aligned}$$

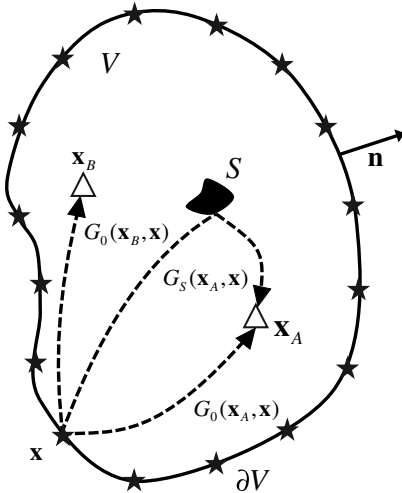


Figure 2. Domain used in the representation theorem, consisting of a volume V , bounded by a surface ∂V with unit outward-pointing normal vector \mathbf{n} . Receivers are placed at \mathbf{x}_A and \mathbf{x}_B : These will be source locations in the wave equations, later converted to receivers by source-receiver reciprocity. The unperturbed medium is represented by a reference medium whereas the perturbed medium is represented by the scattering perturbation S which is added to the reference medium. The dashed arrows denote the stationary paths of (minimum traveltimes paths for) unperturbed waves G^0 propagating between an arbitrary point \mathbf{x} on ∂V and both receivers, and stationary paths of (minimum traveltimes paths for) a perturbed wave G^S propagating between the same arbitrary point \mathbf{x} and the receiver \mathbf{x}_A .

where we assume that perturbations do not occur along the boundary ∂V ($c_{ijkl} = c_{ijkl}^0$), and where I_{00} , I_{0S} , I_{S0} , and I_{SS} denote each of the four terms on the RHS of equation 8 as shown.

The first term on the RHS of equation 8 constitutes one side of the correlation-type representation theorem for the reference medium, thus it equals the reference homogeneous Green's function ($I_{00} = G_{in}^0(\mathbf{x}_B, \mathbf{x}_A) - G_{in}^{0*}(\mathbf{x}_B, \mathbf{x}_A)$). If we bring this term over to the left-hand side (LHS) and we subtract the reference homogeneous Green's function from the total homogeneous Green's function, we obtain

$$\begin{aligned} & G_{in}^S(\mathbf{x}_B, \mathbf{x}_A) - G_{in}^{S*}(\mathbf{x}_B, \mathbf{x}_A) \\ &= \int_{\partial V} \{G_{im}^{0*}(\mathbf{x}_B, \mathbf{x}) n_j c_{mjkl} \partial_k G_{nl}^S(\mathbf{x}_A, \mathbf{x}) \\ &\quad - G_{nm}^S(\mathbf{x}_A, \mathbf{x}) n_j c_{mjkl} \partial_k G_{il}^{0*}(\mathbf{x}_B, \mathbf{x})\} dx^2 \leftarrow I_{0S} \\ &\quad + \int_{\partial V} \{G_{im}^{S*}(\mathbf{x}_B, \mathbf{x}) n_j c_{mjkl} \partial_k G_{nl}^0(\mathbf{x}_A, \mathbf{x}) \\ &\quad - G_{nm}^0(\mathbf{x}_A, \mathbf{x}) n_j c_{mjkl} \partial_k G_{il}^{S*}(\mathbf{x}_B, \mathbf{x})\} dx^2 \leftarrow I_{S0} \\ &\quad + \int_{\partial V} \{G_{im}^{S*}(\mathbf{x}_B, \mathbf{x}) n_j c_{mjkl} \partial_k G_{nl}^S(\mathbf{x}_A, \mathbf{x}) \\ &\quad - G_{nm}^S(\mathbf{x}_A, \mathbf{x}) n_j c_{mjkl} \partial_k G_{il}^{S*}(\mathbf{x}_B, \mathbf{x})\} dx^2 \leftarrow I_{SS}. \quad (9) \end{aligned}$$

This is the correlation-type representation theorem for perturbed elastic media (Lu et al., 2011): The scattered homogeneous Green's function between \mathbf{x}_A and \mathbf{x}_B is given by the sum of three different surface integrals that contain crosscorrelations of reference and perturbed and only perturbed wavefields between the enclosing boundary ∂V and each of these points.

A related result, the derivation of which is based on the theory of reciprocity for perturbed elastic media, can be found in Vasconcelos (2008a) and Gaiser and Vasconcelos (2009). Their equations differ by the fact that only the causal scattered Green's function is constructed (so-called "one-sided theorems") using a combination of surface and volume integrals.

Equation 9 is of great importance for practical applications like imaging because each of the integrals can be computed numerically, and the related contribution can be added together to give a non-linear imaging condition as we show below.

Example 1: 2D acoustic point scattering

To illustrate how the correlation-type representation theorem for perturbed media works, we now implement two simple examples of the acoustic version of this theorem proposed by Fleury and Vasconcelos (2012):

$$\begin{aligned} & G^S(\mathbf{x}_B, \mathbf{x}_A) + G^{S*}(\mathbf{x}_B, \mathbf{x}_A) \\ &= \frac{1}{j\omega\rho} \int_{\partial V} \{G^{0*}(\mathbf{x}_B, \mathbf{x}) \partial_i G^S(\mathbf{x}_A, \mathbf{x}) \\ &\quad - G^S(\mathbf{x}_A, \mathbf{x}) \partial_i G^{0*}(\mathbf{x}_B, \mathbf{x})\} n_i dx^2 \leftarrow \hat{I}_{0S} \\ &\quad + \frac{1}{j\omega\rho} \int_{\partial V} \{G^{S*}(\mathbf{x}_B, \mathbf{x}) \partial_i G^0(\mathbf{x}_A, \mathbf{x}) \\ &\quad - G^0(\mathbf{x}_A, \mathbf{x}) \partial_i G^{S*}(\mathbf{x}_B, \mathbf{x})\} n_i dx^2 \leftarrow \hat{I}_{S0} \\ &\quad + \frac{1}{j\omega\rho} \int_{\partial V} \{G^{S*}(\mathbf{x}_B, \mathbf{x}) \partial_i G^S(\mathbf{x}_A, \mathbf{x}) \\ &\quad - G^S(\mathbf{x}_A, \mathbf{x}) \partial_i G^{S*}(\mathbf{x}_B, \mathbf{x})\} n_i dx^2 \leftarrow \hat{I}_{SS}. \quad (10) \end{aligned}$$

This allows us to discuss in more detail the various contributions of terms on the RHS to the reconstruction of the scattered wavefield between \mathbf{x}_A and \mathbf{x}_B . In the next section, we present an elastic example where equation 9 is implemented for a 2D isotropic elastic medium.

Figure 3 shows an isotropic point scatterer at position \mathbf{x}_S that represents a high-density perturbation to the homogeneous background medium which is of infinite extent with density $\rho = 1000 \text{ kg/m}^3$ and velocity $v = 1500 \text{ m/s}$. The scatterer is surrounded by a closed circular boundary of 800 sources with radius $r = 700 \text{ m}$, and two receivers are also located inside this boundary at a distance of $d = 400 \text{ m}$ from each other. In a first step, separate forward-modeling runs are carried out for each source on the boundary and the wavefield is recorded by both receivers using the unperturbed background velocity model giving $G^0(\mathbf{x}_A, \mathbf{x})$ and $G^0(\mathbf{x}_B, \mathbf{x})$, and their spatial derivatives across boundary ∂V are calculated. In a second step, forward-modeling runs are carried out for each source on the boundary and the wavefield is recorded by both receivers using the perturbed velocity model including the scatterer, giving $G(\mathbf{x}_A, \mathbf{x})$ and $G(\mathbf{x}_B, \mathbf{x})$ and their spatial derivatives. In this example, we use a 2D acoustic finite-difference method to model the wavefield with absorbing boundary condition, and calculate the spatial derivatives by using a finite-difference stencil. The time series are frequency-band limited from 0 to 60 Hz using a Ricker wavelet with a center frequency $f_c = 30 \text{ Hz}$. We then implement separately the crosscorrelation of reference and perturbed wavefields in integrals \hat{l}_{0S} (Figure 4a and 4b) and \hat{l}_{S0} (Figure 4c and 4d) in equation 10, and the crosscorrelation of only perturbed wavefields in integral \hat{l}_{SS} (Figure 4e and 4f). Finally, for comparison with the result of evaluating the RHS of equation 10, we run the forward model between the two receiver locations with the receiver located at \mathbf{x}_A replaced by a source; we use the unperturbed background velocity model and the perturbed model, then we subtract these wavefields to obtain the true scattered Green's function between \mathbf{x}_A and \mathbf{x}_B due to the presence of a point scatterer. This true Green's function represents a (bandlimited) impulse at $t_{\mathbf{x}_A, \mathbf{x}_S} + t_{\mathbf{x}_B, \mathbf{x}_S}$ (Figure 5), where $t_{\mathbf{x}_i, \mathbf{x}_j}$ is the time that the wavefield takes to go from \mathbf{x}_i to \mathbf{x}_j , or vice versa.

A comparison of the true Green's function with the trace obtained by the crosscorrelation of reference and perturbed wavefields in Figure 5 shows that the latter integrals produces an impulse with the correct traveltime (constructed in Figure 6a and 6c) but also another impulse at a traveltime corresponding to $t_{\mathbf{x}_A, \mathbf{x}_S} - t_{\mathbf{x}_B, \mathbf{x}_S}$ (Figure 6b and 6d). This second impulse represents nonphysical energy as discussed more in detail by Snieder et al. (2008), Halliday and Curtis (2009), Wapenaar et al. (2010c), and Douma et al. (2011). Thus, the construction of the scattered Green's function between \mathbf{x}_A and \mathbf{x}_B with the terms \hat{l}_{0S} and \hat{l}_{S0} includes significant spurious energy.

Because the correlation-type representation theorem for perturbed acoustic media (equation 10) is mathematically exact, we expect the remaining integral to provide a contribution that cancel out this nonphysical energy precisely. The crosscorrelation of perturbed wavefields (term \hat{l}_{SS}) is thus fundamental to removing nonphysical energy. This term is nonlinear in the scattered-wave Green's functions, and we will see below that for the same reason as above this nonlinear term also tidies up errors in images, if it can be applied.

A stationary-phase analysis shows that the nonlinear term is stationary everywhere along the boundary ∂V with traveltime equal to

$t_{\mathbf{x}_A, \mathbf{x}_S} - t_{\mathbf{x}_B, \mathbf{x}_S}$ as explained by Figure 7 and by Halliday and Curtis (2009). The trace obtained by the sum of the crosscorrelations of unperturbed and perturbed waves interferes destructively with the trace obtained by the crosscorrelation of only perturbed waves at traveltime $t_{\mathbf{x}_A, \mathbf{x}_S} - t_{\mathbf{x}_B, \mathbf{x}_S}$, and the nonphysical wave is not present in the final result. As predicted by the theory, the trace constructed in Figure 8, by summing all the three terms $\hat{l}_{0S} + \hat{l}_{S0} + \hat{l}_{SS}$ fits the true scattered Green's function perfectly.

In this example, we have chosen a homogeneous infinite medium as reference medium. However, representation theorems for perturbed media do not require any assumptions to be made about the nature of the unperturbed medium which can be anything from homogenous to a complex medium with smooth or sharp boundaries and distributed diffractors. We now extend the numerical example by defining a two-layer medium as the background medium and a point scatterer embedded in the first layer as the perturbation (Figure 9). The analysis of integrands (Figure 10) is not as straightforward as in the previous case because the reference wavefields contain not only the direct arrival but also a single reflected arrival. Furthermore, the wavefield perturbations are composed of the single scattering event plus multiple scattering-reflection arrivals due to repeated interactions of the scattered waves with the boundary in the background medium. Nevertheless, the theory of Green's function construction in perturbed media guarantees that the correlation-type reciprocity theorem reconstructs the scattered Green's function between \mathbf{x}_A and \mathbf{x}_B , and the reconstructed trace in Figure 11 matches the true scattered Green's function perfectly. This trace is composed of four events: a first, at traveltime $t \approx 0.78 \text{ s}$, corresponds to a wave reaching the scatterer before being recorded at \mathbf{x}_B . The second and third events at traveltimes $t \approx 1.19 \text{ s}$ and $t \approx 1.29 \text{ s}$ correspond to a wave interacting with the scatterer and subsequently the reflector, and vice versa. Finally, a fourth weak event at traveltime $t \approx 1.7 \text{ s}$ is due to a wave reaching the scatterer, the reflector, and again the scatterer.

These acoustic examples are important as they are simpler versions of the elastic examples discussed in later sections. They show how the crosscorrelations of reference and perturbed

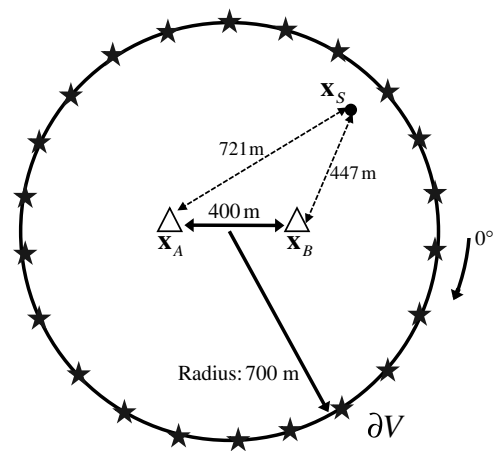


Figure 3. Geometry used for numerical example. Stars indicate sources on the boundary ∂V , triangles indicate receivers, and the scatterer S is represented by a black dot. The background medium is an homogenous medium with density $\rho = 1000 \text{ kg/m}^3$ and velocity $v = 1500 \text{ m/s}$, and the point scatterer S represents a positive density perturbation of $\Delta\rho = 1200 \text{ kg/m}^3$.

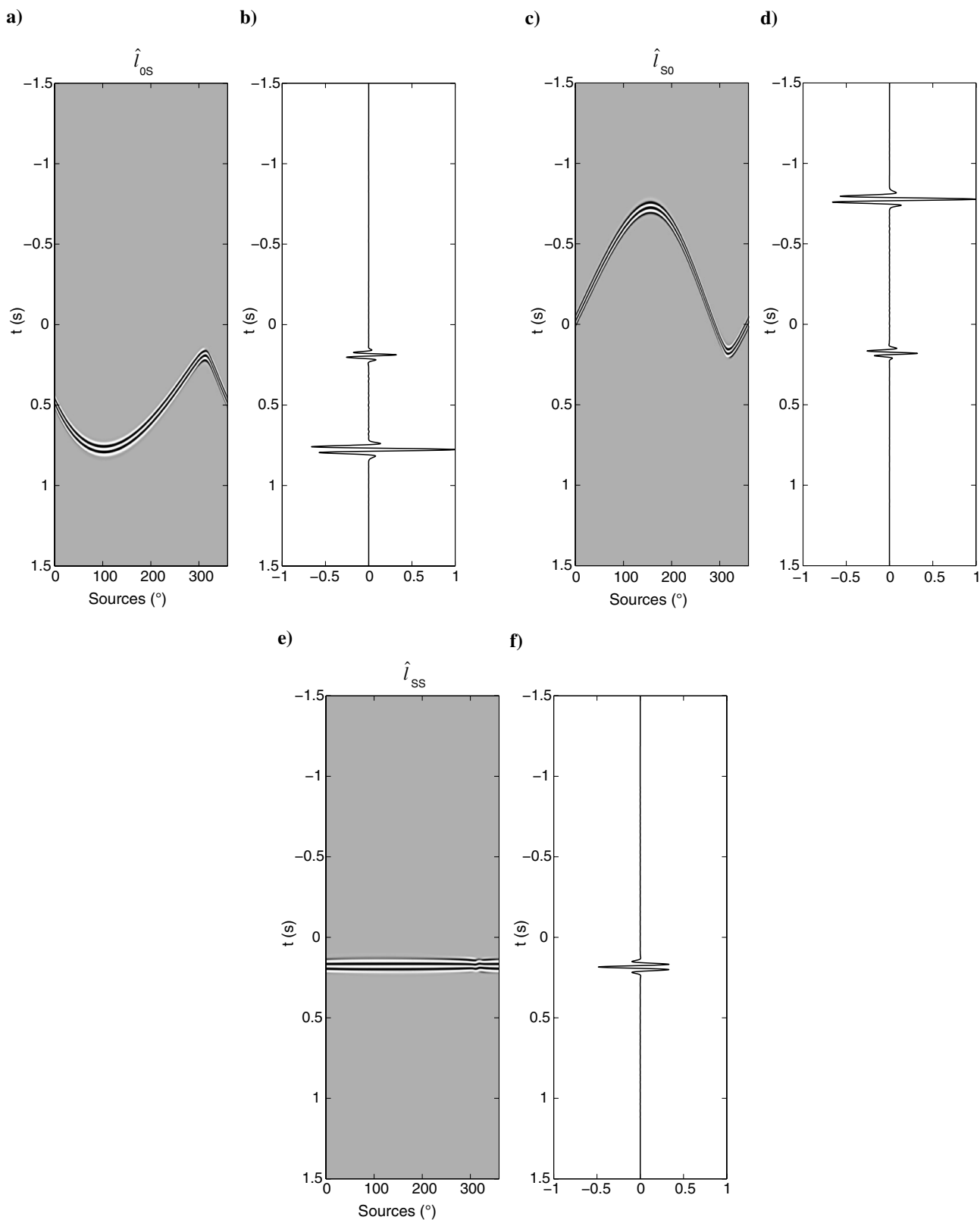


Figure 4. (a) The integrand of \hat{l}_{0S} for the experiment depicted in Figure 3. (b) The sum (integral over receivers) of all traces in (a). (c) The integrand of \hat{l}_{S0} . (d) The sum (integral over receivers) of all traces in (c). (e) The integrand of \hat{l}_{SS} . (f) The sum (integral over receivers) of all traces in (e). Events in (b) and (d) represent the correct (physical) scattered wave between \mathbf{x}_B and \mathbf{x}_A at $t \approx 0.78$ s, plus a nonphysical event at $t = 0.18$ s, whereas the waveform in (f) represents a nonphysical event at $t \approx 0.18$ s which, when added to the sum of the other integrals, will cancel out their spurious energy.

wavefields construct the correct, physical scattered wavefield but also nonphysical waves. The crosscorrelation of only perturbed wavefields perfectly cancels all nonphysical energy. Thus, even though visualization of the different terms that contribute to the construction of the elastic scattered Green's function and a stationary-phase analysis of physical and nonphysical energy (below) are difficult, we also expect, to the same extent, similar behavior for the elastic case.

Example 2: 2D elastic point scattering

In a second example, we apply the theory presented in this paper for perturbed elastic media. An isotropic homogeneous medium with density $\rho = 1000 \text{ kg/m}^3$, compressional wave-velocity $V_P = 1500 \text{ m/s}$, and shear wave-velocity $V_S = 800 \text{ m/s}$ is used as reference medium, and a high-density point perturbation is added to the background medium. Two receivers are surrounded by a square boundary of sources (the distance between sources is $dx_S = 2 \text{ m}$) as shown in Figure 12.

We expect to see reflections (PP and SS) and conversions (PS and SP) between the two receiver locations due to the point scatterer. We construct the scattered Green's function excited by a horizontal body-force source at location \mathbf{x}_A and recorded by a horizontal particle velocity receiver at location \mathbf{x}_B , where velocity recordings are given by $\dot{G}_{xx}^S(\mathbf{x}_B, \mathbf{x}_A, t) = \frac{d}{dt} G_{xx}^S(\mathbf{x}_B, \mathbf{x}_A, t)$ because Green's functions G are displacement Green's functions. Because a body-force density source excites P-waves as well as S-waves, this Green's function is mainly composed of four events: The first and the fourth events are due to the PP and SS pure scattering, whereas the second and the third events are the PS and SP conversions (Figure 13 — red line).

Again, in a first step, separate forward-modeling runs are carried out using the unperturbed background velocity model, and in a second step forward-modeling runs are carried out using the perturbed velocity model. We then run the forward model also with the receiver located at \mathbf{x}_A replaced by a source, using the unperturbed background velocity model and the perturbed one, and we subtract these wavefields to obtain the true scattered wave Green's function $\dot{G}_{xx}^S(\mathbf{x}_B, \mathbf{x}_A, t)$ between \mathbf{x}_A and \mathbf{x}_B due to the presence of the scatterer. The time series are frequency-band limited from 0 to 60 Hz using a Ricker wavelet with a center frequency $f_c = 30 \text{ Hz}$. Forward-modeling simulations are performed using a staggered-grid, 2D elastic finite-difference algorithm (Robertsson et al., 1994). Outgoing (i.e., radiation or absorbing) boundary conditions are applied just outside the surface enclosing the points of interest to truncate the computational domain, and the wavefield is recorded by both receivers. Because we consider the 2D elastodynamic wave equation, at least two forward simulations must be accomplished for each source location — one for each point-force source in mutually orthogonal directions. According to equation 9, derivatives of the Green's function with respect to the source location on the boundary must also be computed. However, using reciprocity, these terms also can be interpreted as the traction measured on the enclosing boundary resulting from point forces at any particular point of interest, and traction may be derived directly from the finite-difference modeling results because the code is based on a velocity-stress formulation. In the following, particle velocity Green's tensors are used and the interferometric Green's functions are computed after taking the time derivative of the interferometric integral 9.

After these wavefields are computed, we implement the interferometric integrals. The trace obtained by the crosscorrelations of

reference and perturbed wavefields (Figure 13) shows eight events, exactly twice the number of events we expect from the physical events. Four of them are physical events with traveltimes equal to the sum of any combination of P- and S-waves traveling from \mathbf{x}_A to the scatterer and from the scatterer to \mathbf{x}_B (Figure 14), whereas the others are spurious or nonphysical events with traveltimes equal to the difference of any combination of P- and S-waves traveling from \mathbf{x}_A to the scatterer and from the scatterer to \mathbf{x}_B (Figure 15). However, as already seen in detail for the acoustic case, the crosscorrelation of only perturbed waves cancels out these nonphysical waves, and the seismic trace in Figure 16a fits the true scattered Green's function perfectly. This time series presents the weakest event at earliest time due to the PP wave (traveltime

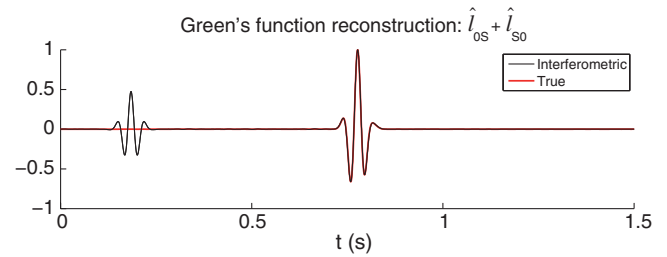


Figure 5. Green's function partial reconstruction with only cross-correlations of reference and perturbed wavefields (black line) and the true scattered Green's function (red line). The partial reconstruction shows a strong nonphysical event at traveltimes $t_{x_S} - t_{x_S} \approx 0.78 \text{ s}$.

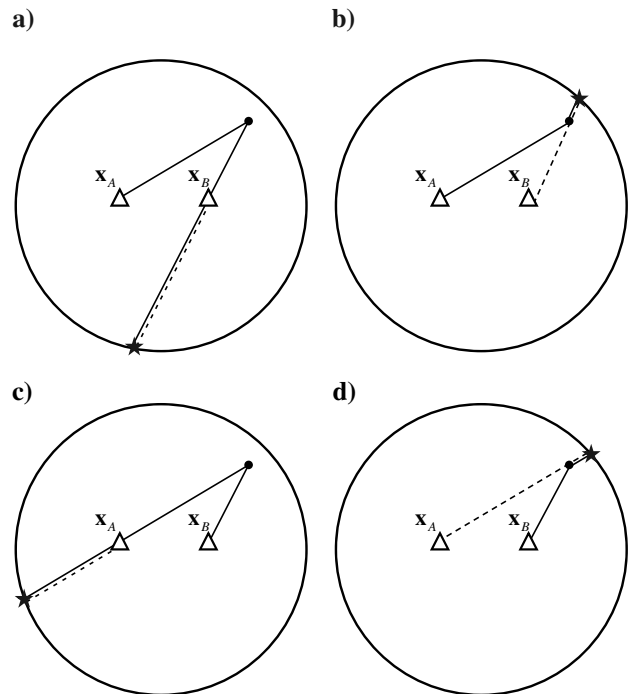


Figure 6. Stationary points in the crosscorrelations of reference and perturbed wavefields \hat{l}_{OS} (top) and \hat{l}_{SO} (bottom). Solid lines represent stationary paths of the scattered Green's function G^S . Dotted lines represent stationary paths of the reference Green's function G^0 that is time-reversed and crosscorrelated with the scattered Green's function. (a) and (c) correspond to the construction of a stationary physical event, the scattered wave between \mathbf{x}_B and \mathbf{x}_A . (b) and (d) correspond to the construction of a stationary nonphysical event.

$t_{\mathbf{x}_A, \mathbf{x}_B}^{PP} = t_{\mathbf{x}_A, \mathbf{x}_S}^P + t_{\mathbf{x}_B, \mathbf{x}_S}^P \approx 0.44$ s), and the strongest event at latest time due to the SS wave ($t_{\mathbf{x}_A, \mathbf{x}_B}^{SS} = t_{\mathbf{x}_A, \mathbf{x}_S}^S + t_{\mathbf{x}_B, \mathbf{x}_S}^S \approx 0.82$ s); the two intermediate events come from conversion of a P-wave into an S-wave ($t_{\mathbf{x}_A, \mathbf{x}_B}^{PS} = t_{\mathbf{x}_A, \mathbf{x}_S}^P + t_{\mathbf{x}_B, \mathbf{x}_S}^S \approx 0.58$ s) and vice versa ($t_{\mathbf{x}_A, \mathbf{x}_B}^{SP} = t_{\mathbf{x}_A, \mathbf{x}_S}^S + t_{\mathbf{x}_B, \mathbf{x}_S}^P \approx 0.67$ s).

We repeat the same procedure to obtain the three other components of the particle velocity Green's tensor $\hat{G}_{zx}^S(\mathbf{x}_B, \mathbf{x}_A, t)$, $\hat{G}_{xz}^S(\mathbf{x}_B, \mathbf{x}_A, t)$, and $\hat{G}_{zz}^S(\mathbf{x}_B, \mathbf{x}_A, t)$, and these are shown in Figure 16. Note how the different source-radiation patterns are reproduced accurately. The cancellation of nonphysical energy occurs in exactly the same way as above for each of these terms.

REPRESENTATION THEOREMS FOR PERTURBED ELASTIC MEDIA FOR P- AND S-WAVES

As shown above, the final reconstructed Green's functions can be understood in terms of P- and S-waves and their conversions. A similar understanding of the internal process of crosscorrelation within the integrals of equation 9 might be tractable if we understood how P- and S-waves interact within these integrals. We therefore now derive a correlation-type representation theorem in perturbed elastic media in terms of P- and S-waves, rather than only in terms of displacement-type Green's functions as above (equation 9).

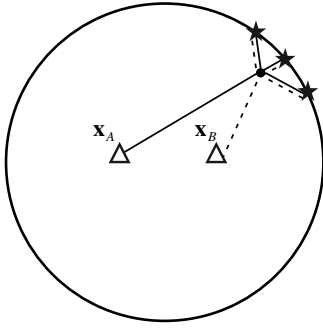


Figure 7. Stationary points in the crosscorrelation between only scattered waves (Figure 4e), creating a nonphysical event that cancels out the spurious energy in Figure 5.

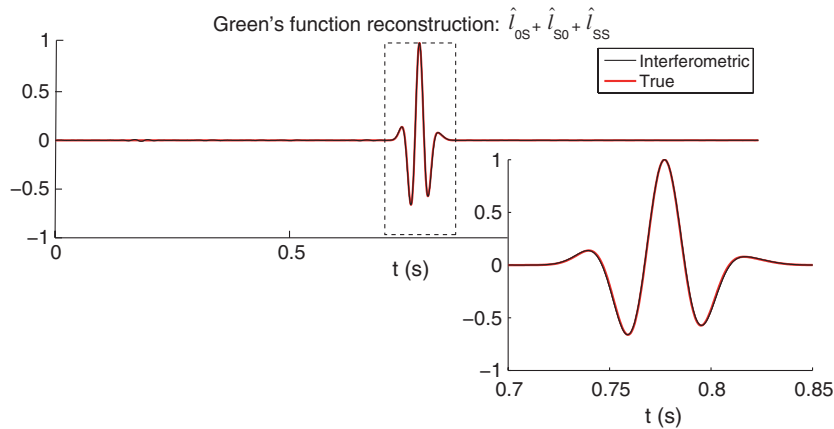


Figure 8. Green's function full reconstruction including all integrands in equation 10 (black line), and the true scattered Green's function (red line). The insert shows a detail of the main arrival. The full reconstruction is perfect and the spurious energy due to the surface integral has been canceled out by the crosscorrelation between scattered waves.

Taking advantage of the P- and S-wave Green's functions defined by Wapenaar and Haimé (1990) and Wapenaar and Fokkema (2006), we recall that the P- and S-wave components of the wavefield can be expressed as a sum of partial derivatives of the displacement

$$G_{\psi_0 n}(\mathbf{x}_B, \mathbf{x}_A) = -\rho c_P^2 \partial_i G_{in}(\mathbf{x}_B, \mathbf{x}_A) \quad (11)$$

$$G_{\psi_{kn}}(\mathbf{x}_B, \mathbf{x}_A) = -\rho c_S^2 \varepsilon_{kji} \partial_i G_{in}(\mathbf{x}_B, \mathbf{x}_A), \quad (12)$$

where c_P and c_S are, respectively, the local P-wave and S-wave velocities at \mathbf{x}_B , $G_{\psi_0 n}(\mathbf{x}_B, \mathbf{x}_A)$ is the Green's function representing the P-wave at \mathbf{x}_B , $G_{\psi_{kn}}(\mathbf{x}_B, \mathbf{x}_A)$ is the equivalent Green's function representing the S-wave at \mathbf{x}_B polarized in the plane with normal n_k , and ε_{kji} is the alternating tensor (or Levi-Civita tensor). We use the notation $G_{\psi_{Kn}}(\mathbf{x}_B, \mathbf{x}_A)$ with K equal to 0, 1, 2, or 3. $K = 0$ refers to the P-wave and $K = 1, 2$ or 3 refers to the S-wave with orthogonal orientations, assuming that appropriate P or S velocities are used in equations 11 and 12. Note that, to interpret these equations as P- and S-waves, we are assuming that the medium is homogenous and isotropic locally around the receiver point \mathbf{x}_B . Furthermore, even though the application of the divergence and curl to the full particle displacement vector is always valid, their respective definition as P- and S-waves (and their conversions) is only valid in the far-field region (Wu and Ben-Menahem, 1985).

Equations 11 and 12 are weighted sums of the spatial derivatives of point force responses and can be used to express P- and S-wave source and receiver Green's functions by taking derivatives of equation 9 (Halliday et al., 2012)

$$\begin{aligned} & G_{\psi_i \psi_n}^S(\mathbf{x}_B, \mathbf{x}_A) - G_{\psi_i \psi_n}^{S*}(\mathbf{x}_B, \mathbf{x}_A) \\ &= \int_{\partial V} \{ G_{\psi_i m}^{0*}(\mathbf{x}_B, \mathbf{x}) n_j c_{mjkl} \partial_k G_{\psi_n l}^S(\mathbf{x}_A, \mathbf{x}) \\ &\quad - G_{\psi_n m}^S(\mathbf{x}_A, \mathbf{x}) n_j c_{mjkl} \partial_k G_{\psi_i l}^{0*}(\mathbf{x}_B, \mathbf{x}) \} dx^2 \\ &+ \int_{\partial V} \{ G_{\psi_i m}^{S*}(\mathbf{x}_B, \mathbf{x}) n_j c_{mjkl} \partial_k G_{\psi_n l}^0(\mathbf{x}_A, \mathbf{x}) \\ &\quad - G_{\psi_n m}^0(\mathbf{x}_A, \mathbf{x}) n_j c_{mjkl} \partial_k G_{\psi_i l}^{S*}(\mathbf{x}_B, \mathbf{x}) \} dx^2 \\ &+ \int_{\partial V} \{ G_{\psi_i m}^{S*}(\mathbf{x}_B, \mathbf{x}) n_j c_{mjkl} \partial_k G_{\psi_n l}^S(\mathbf{x}_A, \mathbf{x}) \\ &\quad - G_{\psi_n m}^S(\mathbf{x}_A, \mathbf{x}) n_j c_{mjkl} \partial_k G_{\psi_i l}^{S*}(\mathbf{x}_B, \mathbf{x}) \} dx^2. \quad (13) \end{aligned}$$

This representation theorem for perturbed elastic media shows how $G_{\psi_i \psi_n}^S(\mathbf{x}_B, \mathbf{x}_A)$, the Green's function representing the P- or S-wave component of the scattered wavefield at \mathbf{x}_B due to a P- or S-wave source at \mathbf{x}_A , can be recovered from reference and perturbed Green's functions between \mathbf{x}_i ($i = A, B$) and the enclosing boundary ∂V representing the P- or S-wave components of the wavefield due to force and deformation point sources at boundary points $\mathbf{x} \in \partial V$.

In land acquisition, the most advanced multi-component seismic survey gives a total of nine components for analysis (9C data). This uses one vertical and two orthogonal S-wave vibrators (or one triaxial vibrator) as sources, and records P-waves and S-waves by deploying multi-component receivers that measure particle displacements in three perpendicular orientations. This

configuration is well-suited to use the representation theorem for perturbed elastic media (equation 13) because using the appropriate combination of recordings (e.g., for a P-wave generated by a vertical point force, use $G_{\psi_0 z}^{0/S}(\mathbf{x}_i, \mathbf{x})$) we can estimate any combination of P- and S-waves (PP, PS, SP, and SS) propagating between the two receiver locations \mathbf{x}_A and \mathbf{x}_B . For example, considering again the geometry in Figure 12, we compute P- or S-wave recordings at \mathbf{x}_A and \mathbf{x}_B , from vertical and horizontal sources on boundary ∂V . These recordings are combined to compute the scattered wave representing the P- or S-wave components of the wavefield at \mathbf{x}_B due to a P- or S-wave source at \mathbf{x}_A and the reconstruction is nearly perfect (Figure 17 — differences are due to numerical errors only). Of course, in practical applications, the estimate is limited by only having sources on the earth's surface (rather than on an enclosing boundary) so the reconstruction will be affected by some nonphysical artifacts. Nevertheless, equation 13 does show how P- or S-waves are constructed from force and deformation point sources, and allows the effect of a depletion of the surface integrals to span only the earth's surface, to be analyzed for land seismic surveys.

In a marine environment, on the other hand, water cannot transmit shear wave energy. Marine multicomponent recording of shear energy is only feasible using ocean-bottom seismometers (OBSs). Furthermore, marine seismic airguns can generate only P-wave energy. According to these constraints, the representation theorem for perturbed elastic media (equation 13) cannot be used directly. We use the transformation proposed by Wapenaar and Fokkema (2006) to change source quantities on ∂V to be P- and S-wave sources. Assuming that the medium at, and outside of ∂V is homogeneous, isotropic, and unperturbed, by expressing force and deformation sources in term of sources of P- and S-wave potentials, we obtain

$$\begin{aligned}
 &G_{\psi_i \psi_N}^S(\mathbf{x}_B, \mathbf{x}_A) + G_{\psi_i \psi_N}^{S*}(\mathbf{x}_B, \mathbf{x}_A) \\
 &= \frac{2}{j\omega\rho} \int_{\partial V} \{ \partial_j G_{\psi_i \psi_K}^0(\mathbf{x}_B, \mathbf{x}) \}^* G_{\psi_N \psi_K}^S(\mathbf{x}_A, \mathbf{x}) n_j dx^2 \\
 &\quad + \frac{2}{j\omega\rho} \int_{\partial V} \{ \partial_j G_{\psi_i \psi_K}^S(\mathbf{x}_B, \mathbf{x}) \}^* G_{\psi_N \psi_K}^0(\mathbf{x}_A, \mathbf{x}) n_j dx^2 \\
 &\quad + \frac{2}{j\omega\rho} \int_{\partial V} \{ \partial_j G_{\psi_i \psi_K}^S(\mathbf{x}_B, \mathbf{x}) \}^* G_{\psi_N \psi_K}^S(\mathbf{x}_A, \mathbf{x}) n_j dx^2. \quad (14)
 \end{aligned}$$

This equation still requires the availability of monopole and dipole P- and S-wave source responses. If only monopole responses are available, we approximate the dipole response using $\partial_j G_{\psi_i \psi_K}^{0/S}(\mathbf{x}_B, \mathbf{x}) n_j \approx -(j\omega/c_K) G_{\psi_i \psi_K}^{0/S}(\mathbf{x}_B, \mathbf{x})$, where c_K is either the P- or S-wave velocity as appropriate, to obtain

$$\begin{aligned}
 &G_{\psi_i \psi_N}^S(\mathbf{x}_B, \mathbf{x}_A) + G_{\psi_i \psi_N}^{S*}(\mathbf{x}_B, \mathbf{x}_A) \\
 &\approx \frac{2}{\rho c_K} \int_{\partial V} G_{\psi_i \psi_K}^{0*}(\mathbf{x}_B, \mathbf{x}) G_{\psi_N \psi_K}^S(\mathbf{x}_A, \mathbf{x}) dx^2 \\
 &\quad + \frac{2}{\rho c_K} \int_{\partial V} G_{\psi_i \psi_K}^{S*}(\mathbf{x}_B, \mathbf{x}) G_{\psi_N \psi_K}^0(\mathbf{x}_A, \mathbf{x}) dx^2 \\
 &\quad + \frac{2}{\rho c_K} \int_{\partial V} G_{\psi_i \psi_K}^{S*}(\mathbf{x}_B, \mathbf{x}) G_{\psi_N \psi_K}^S(\mathbf{x}_A, \mathbf{x}) dx^2. \quad (15)
 \end{aligned}$$

The Green's function representing the scattered P- or S-wave component of the wavefield at \mathbf{x}_B due to a P- or S-wave source at \mathbf{x}_A ($G_{\psi_i \psi_N}^S(\mathbf{x}_B, \mathbf{x}_A)$) can be recovered using only Green's functions from a boundary of P- or S-wave sources at $\mathbf{x} \in \partial V$ representing

the unperturbed and perturbed P- or S-wave components of the wavefield at $\mathbf{x}_i (i = A, B)$ (Gaiser and Vasconcelos, 2009). Equation 15 can be used for instance to examine the effects of depleting the boundary sources to be P-sources only, as is required in marine seismic surveys.

GENERALIZED FORM OF IMAGING CONDITION WITH SCALAR AND VECTOR POTENTIALS

As summarized in the Introduction, seismic-migration algorithms that use numerical solutions of the wave equation to produce an image of the subsurface generally consist of two consecutive steps: subsurface wavefield reconstruction, followed by the application of an imaging condition. For prestack depth migration, source and receiver wavefields must be reconstructed at all locations in the subsurface given the true recorded receiver and injected source fields in the actual survey. Using recorded data as boundary conditions, an imaging condition is then applied at all locations in the subsurface, which is supposed to discriminate places where the up- and down-going wavefields (actually by assumption, the incident and scattered wavefields) are directly related (through local perturbations to the medium), and those where they are not. Thus we obtain an "image" of the perturbations.

The simplest imaging conditions are based on crosscorrelation or deconvolution of the reconstructed wavefields (Claerbout, 1971, 1985). Vasconcelos et al. (2009a) and Halliday and Curtis (2010) pointed out that there is a connection between the wavefield correlations performed in seismic imaging and those performed in the theory and practice of seismic interferometry. In particular, acoustic representation theorems for the scattered field contain surface integrals similar to those in seismic imaging. Because an image of a scatterer can be obtained by extrapolating the recorded scattered wavefield back to the scatterer location and evaluating it at zero-time (Vasconcelos et al., 2009a), a formulation based on scattering representations can be used to interpret the imaging condition in the context of seismic interferometry. However, typical implementations of two-way imaging by, for example, reverse-time migration do not use complete formulations of such an imaging

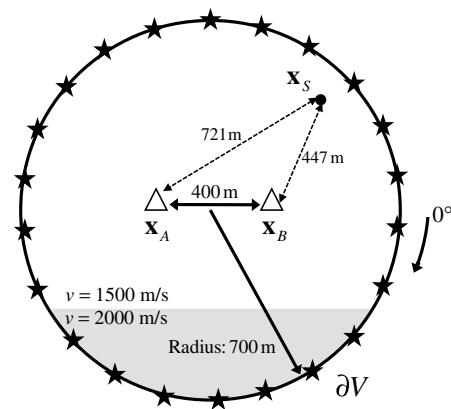


Figure 9. Geometry used for the numerical example. Stars indicate sources on the boundary ∂V , triangles indicate receivers and the scatterer is represented by a black dot. The background medium is composed of two layers, the top one with velocity $v = 1500$ m/s, the bottom one with $v = 2000$ m/s. A point scatterer is added as a positive density perturbation of $\Delta\rho = 1200$ kg/m³ to a homogenous density model ($\rho = 1000$ kg/m³).

condition. The gradient terms in the surface integrands above, that require data to be acquired with monopole and dipole sources and receivers, are approximated by invoking the far-field approximation $\partial_i G n_i = (j\omega/c) G$. Moreover, the volume integrals that account for dynamic and kinematic effects associated with (e.g., forward scattering (i.e., transmission effects and multiple scattering or nonlinear interactions of the fields G^0 and G^S with the potential V) are not implemented in usual imaging methods.

We now examine the relation between the elastic representation theorems above and existing elastic imaging conditions. Starting from equation 13, we apply approximations similar to those in Vasconcelos et al. (2009a) and Halliday and Curtis (2010) to show that the elastic imaging condition with scalar and vector potentials proposed by Yan and Sava (2008) is just an approximated version of the more general representation theorems for perturbed elastic media for P- and S-waves. This is important as it means that the full theory above can be used to understand why the latter algorithm produces imperfect results, and second to indicate ways elastic imaging might be implemented in future.

First, we define a point in the subsurface $\mathbf{x}_P = \mathbf{x}_A = \mathbf{x}_B$ at which we would like to construct an image. The representation theorem for perturbed elastic media (equation 13) becomes

$$\begin{aligned}
 &G_{\psi_l \psi_N}^S(\mathbf{x}_P) - G_{\psi_l \psi_N}^{S*}(\mathbf{x}_P) \\
 &= \int_{\partial V} \{ G_{\psi_l m}^{0*}(\mathbf{x}_P, \mathbf{x}) n_j c_{mjkl} \partial_k G_{\psi_N l}^S(\mathbf{x}_P, \mathbf{x}) \\
 &\quad - G_{\psi_N m}^S(\mathbf{x}_P, \mathbf{x}) n_j c_{mjkl} \partial_k G_{\psi_l}^{0*}(\mathbf{x}_P, \mathbf{x}) \} dx^2 \\
 &\quad + \int_{\partial V} \{ G_{\psi_l m}^{S*}(\mathbf{x}_P, \mathbf{x}) n_j c_{mjkl} \partial_k G_{\psi_N l}^0(\mathbf{x}_P, \mathbf{x}) \\
 &\quad - G_{\psi_N m}^0(\mathbf{x}_P, \mathbf{x}) n_j c_{mjkl} \partial_k G_{\psi_l}^{S*}(\mathbf{x}_P, \mathbf{x}) \} dx^2 \\
 &\quad + \int_{\partial V} \{ G_{\psi_l m}^{S*}(\mathbf{x}_P, \mathbf{x}) n_j c_{mjkl} \partial_k G_{\psi_N l}^S(\mathbf{x}_P, \mathbf{x}) \\
 &\quad - G_{\psi_N m}^S(\mathbf{x}_P, \mathbf{x}) n_j c_{mjkl} \partial_k G_{\psi_l}^{S*}(\mathbf{x}_P, \mathbf{x}) \} dx^2 \quad (16)
 \end{aligned}$$

where $G_{\psi_l \psi_N}^S(\mathbf{x}_P) = G_{\psi_l \psi_N}^S(\mathbf{x}_P, \mathbf{x}_P)$ is the “reflectivity” Green’s function at \mathbf{x}_P , that is, the received scattered P- or S-wave (ψ_l) recorded at point \mathbf{x}_P due to a P- or S-wave source (ψ_N) also located at \mathbf{x}_P . The value of $G_{\psi_l \psi_N}^S(\mathbf{x}_P)$ at zero-time is the instantaneous scattered wave created by a source at \mathbf{x}_P . This can only be nonzero if there is a medium perturbation at \mathbf{x}_P . Hence, this zero-time value is a good candidate to be used as an imaging condition. Note that,

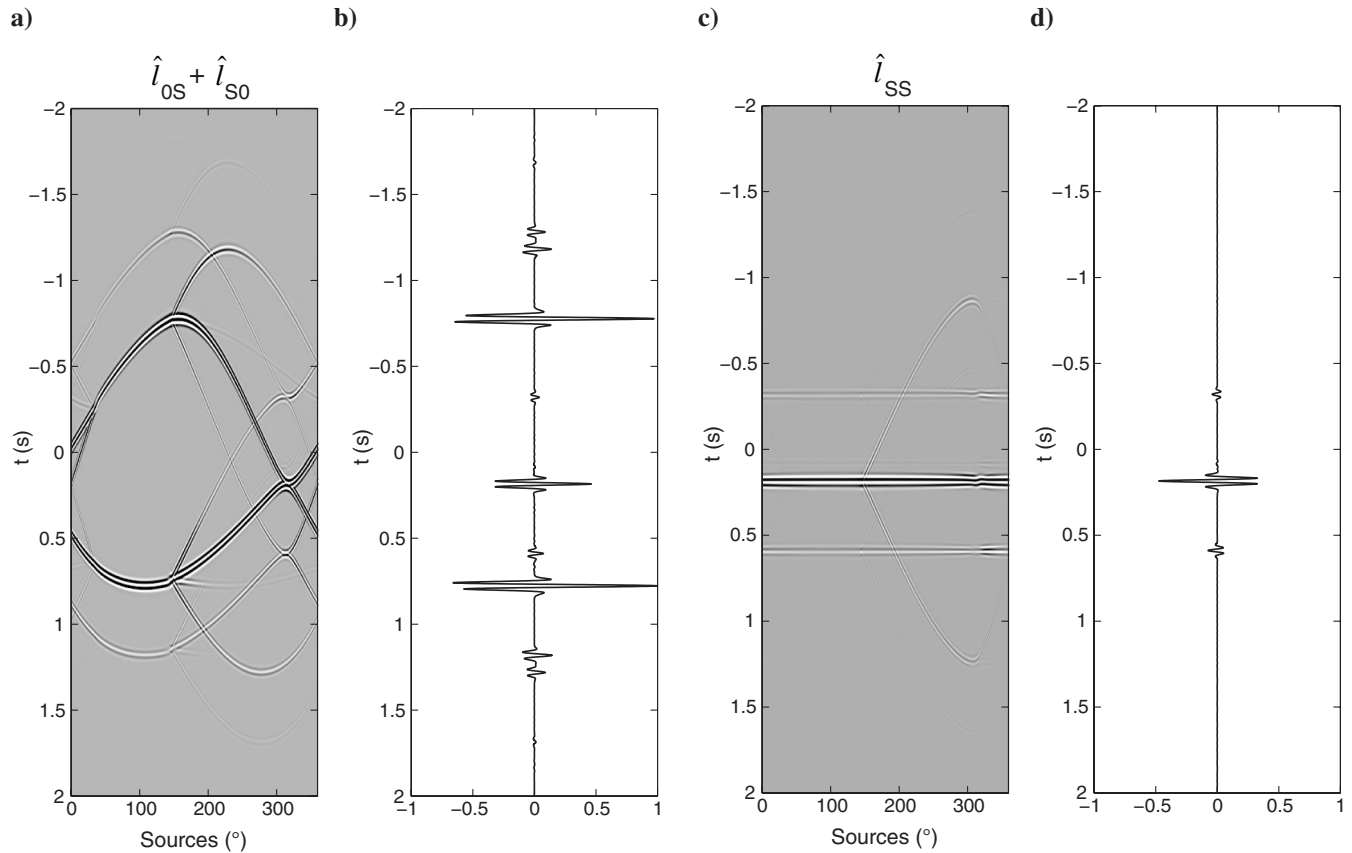


Figure 10. (a) The integrand of $\hat{l}_{0S} + \hat{l}_{S0}$ for the experiment depicted in Figure 9. (b) The sum (integral over receivers) of all traces in (a). (c) The integrand of \hat{l}_{SS} for the experiment depicted in Figure 9. (d) The sum (integral over receivers) of all traces in (c). The crosscorrelation between scattered fields results in three main stationary events, visible in the integrand and the corresponding trace. The first, at traveltimes $t \approx -0.35$ s, is due to the crosscorrelation between waves that are scattered by the diffractor and recorded by the two receivers. When a wave interacting with the reflector and subsequently the scatterer before being recorded at \mathbf{x}_B is crosscorrelated with a wave scattered by the diffractor and recorded at \mathbf{x}_A , a stationary event is created at traveltimes $t \approx 0.18$ s. Finally, if the wave reaching the reflector and subsequently the scatterer before being recorded at \mathbf{x}_A is correlated with the wave scattered by the diffractor and recorded at \mathbf{x}_B , a stationary event is created at traveltimes $t \approx 0.6$ s.

because P- and S-waves (and their conversions) are fully defined only in the far-field, $G_{\psi_l\psi_N}^S(\mathbf{x}_P)$ can be considered only as a near-field projection of the far-field P- and S-waves traveling toward (or leaving) \mathbf{x}_P , that we crosscorrelate to construct the Green's function at \mathbf{x}_P .

To evaluate the integral expression on the RHS of equation 16, we must first compute the subsurface-domain extrapolated wavefields present in the integrands. The source wavefields $G_{\psi_l M}^0(\mathbf{x}_P, \mathbf{x})$ on the RHS of equation 16 are extrapolated in depth from the surface (\mathbf{x}) to \mathbf{x}_P : these are found in practice by solving the elastic wave equation numerically using the m th component of the body-force density as a source, while the receiver wavefields $G_{\psi_N m}^S(\mathbf{x}_P, \mathbf{x})$ are depth-extrapolated numerically by solving a boundary-value problem for the elastic wave equation where the boundary condition (BC) consists of $\mathbf{u}^{S*}(\mathbf{x}_R, \mathbf{x})$, the full, time-reversed scattered wavefield from the acquired common shot data. For both extrapolations, the separation of P- and S-wave potentials is performed in the subsurface, just before the reciprocity-based imaging condition obtained from, for example, the zero-time element of the LHS of equation 16, is calculated.

Integrating over frequencies (ω) to get the zero-time response, we obtain

$$\begin{aligned}
 I_{\psi_N\psi_l, \text{full}}(\mathbf{x}_P) &= 2 \int_0^{+\infty} \text{Re}\{G_{\psi_l\psi_N}^S(\mathbf{x}_P)\}d\omega \\
 &= \int_0^{+\infty} \frac{1}{j\omega} \int_{\partial V} G_{\psi_l m}^{0*}(\mathbf{x}_P, \mathbf{x}) n_j c_{mjkl}^0 \partial_k G_{\psi_N l}^S(\mathbf{x}_P, \mathbf{x}) \\
 &\quad - G_{\psi_N m}^S(\mathbf{x}_P, \mathbf{x}) n_j c_{mjkl}^0 \partial_k G_{\psi_l}^{0*}(\mathbf{x}_P, \mathbf{x}) dx^2 d\omega \\
 &\quad + \int_0^{+\infty} \frac{1}{j\omega} \int_{\partial V} G_{\psi_l m}^{S*}(\mathbf{x}_P, \mathbf{x}) n_j c_{mjkl}^0 \partial_k G_{\psi_N l}^0(\mathbf{x}_P, \mathbf{x}) \\
 &\quad - G_{\psi_N m}^0(\mathbf{x}_P, \mathbf{x}) n_j c_{mjkl}^0 \partial_k G_{\psi_l}^{S*}(\mathbf{x}_P, \mathbf{x}) dx^2 d\omega \\
 &\quad + \int_0^{+\infty} \frac{1}{j\omega} \int_{\partial V} G_{\psi_l m}^{S*}(\mathbf{x}_P, \mathbf{x}) n_j c_{mjkl}^0 \partial_k G_{\psi_N l}^S(\mathbf{x}_P, \mathbf{x}) \\
 &\quad - G_{\psi_N m}^S(\mathbf{x}_P, \mathbf{x}) n_j c_{mjkl}^0 \partial_k G_{\psi_l}^{S*}(\mathbf{x}_P, \mathbf{x}) dx^2 d\omega, \quad (17)
 \end{aligned}$$

where we have expressed every Green's function in terms of particle velocity (Wapenaar and Fokkema, 2006) rather than particle displacement to have the sum (rather than the difference) of the scattered Green's function and its time-reverse (or equivalently in the frequency domain: $\text{Re}\{G_{\text{in}}^S(\mathbf{x}_P)\} = G_{\text{in}}^S(\mathbf{x}_P) + G_{\text{in}}^{S*}(\mathbf{x}_P)$) on the left side. This equation can be regarded as a nonlinear, "true-amplitude" (under ideal acquisition geometries) imaging condition, that accounts also for multiply scattered waves and multiple conversions. It is suitable for land seismic acquisition where body-force density sources directed along x - or z -axes can be used.

Because the formulation with force and deformation sources is not practical for marine ocean-bottom applications and only P-wave sources are usually available, equation 15 is also recast in an imaging context

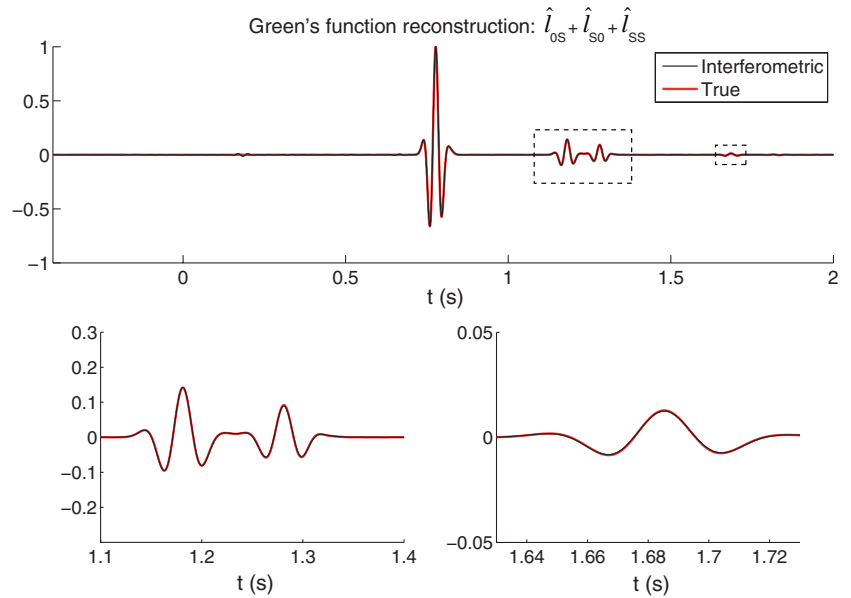


Figure 11. Green's function reconstruction including the crosscorrelation between reference and scattered waves and the crosscorrelation between only scattered waves (black line), and true scattered Green's function (red line). The first insert shows two arrivals: The event at traveltime $t \approx 1.19$ s corresponds to a wave reaching the scatterer and the reflector before being recorded at \mathbf{x}_B , whereas the event at traveltime $t \approx 1.29$ s corresponds to a wave reaching the reflector and subsequently the scatterer. A third weak event due to a wave reaching the scatterer, the reflector and again the scatterer is shown in the second insert. The reconstruction is perfect and the spurious energy due to the integrals observed in Figure 10a has been canceled out by the crosscorrelation between scattered waves.

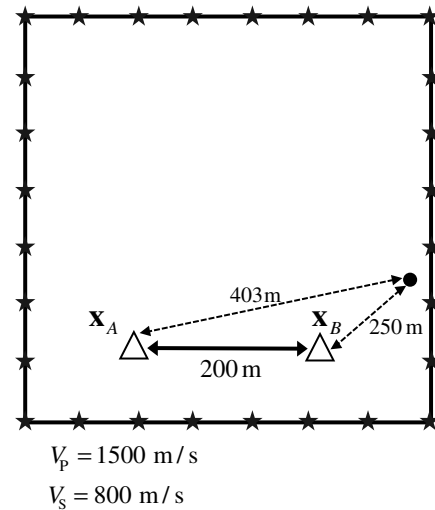


Figure 12. Geometry used for the numerical example. Stars indicate sources on the boundary ∂V , triangles indicate receivers, and the scatterer is represented by a black dot. The background medium is an elastic isotropic homogenous medium with density $\rho = 1000 \text{ kg/m}^3$ and velocities $V_P = 1500 \text{ m/s}$ and $V_S = 800 \text{ m/s}$. A point scatterer ($\Delta\rho = 2000 \text{ kg/m}^3$) is added to the density model.

$$\begin{aligned}
I_{\psi_N \psi_I, \text{full}}(\mathbf{x}_P) &\approx \frac{2}{\rho c_K} \int_0^{+\infty} \int_{\partial V} G_{\psi_I \psi_K}^{0*}(\mathbf{x}_P, \mathbf{x}) G_{\psi_N \psi_K}^S(\mathbf{x}_P, \mathbf{x}) dx^2 d\omega \\
&+ \frac{2}{\rho c_K} \int_0^{+\infty} \int_{\partial V} G_{\psi_I \psi_K}^{S*}(\mathbf{x}_P, \mathbf{x}) G_{\psi_N \psi_K}^0(\mathbf{x}_P, \mathbf{x}) dx^2 d\omega \\
&+ \frac{2}{\rho c_K} \int_0^{+\infty} \int_{\partial V} G_{\psi_I \psi_K}^{S*}(\mathbf{x}_P, \mathbf{x}) G_{\psi_N \psi_K}^S(\mathbf{x}_P, \mathbf{x}) dx^2 d\omega. \quad (18)
\end{aligned}$$

Equation 18 can be considered to be a second, nonlinear (almost) “true-amplitude” imaging condition, suitable for marine ocean-bottom seismic acquisition. The word “almost” reminds us that, be-

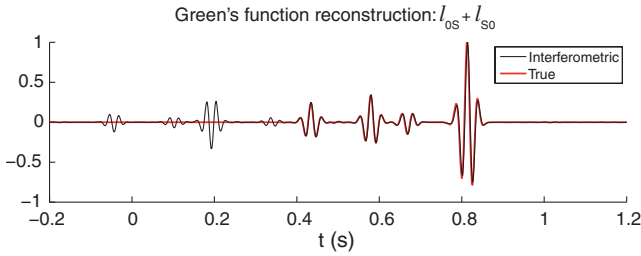


Figure 13. Particle velocity Green's tensor partial reconstruction with only crosscorrelation of reference and perturbed wavefields (black line), and the true scattered Green's function (red line). The partial reconstruction shows four strong nonphysical events at traveltimes $t_{\mathbf{x}_A, \mathbf{x}_S}^{P/S} - t_{\mathbf{x}_B, \mathbf{x}_S}^{P/S}$ as explained by Figure 15.

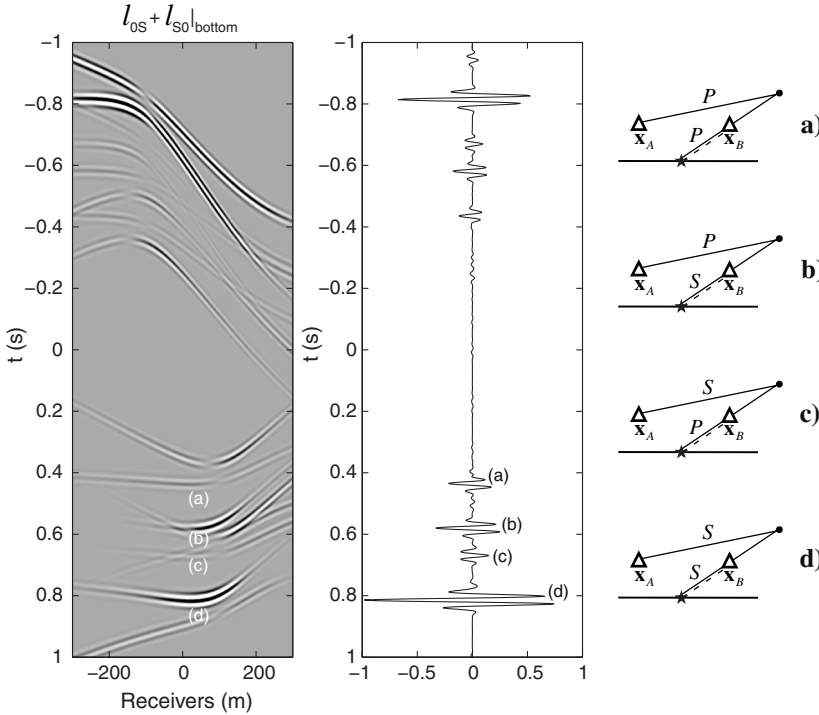


Figure 14. Integrand and stationary points in the crosscorrelation of reference and perturbed wavefields ($l_{OS} + l_{SO}$) that contribute to the generation of physical events in Figure 13. They have a traveltime equal to the sum of (a) P-waves traveling from \mathbf{x}_A to the scatterer and from the scatterer to \mathbf{x}_B , (b) P-waves traveling from \mathbf{x}_A to the scatterer and S-waves traveling from the scatterer to \mathbf{x}_B , (c) S-waves traveling from \mathbf{x}_A to the scatterer and P-waves traveling from the scatterer to \mathbf{x}_B , and (d) S-waves traveling from \mathbf{x}_A to the scatterer and from the scatterer to \mathbf{x}_B .

cause only monopole sources are used, the boundary ∂V must be approximately spherical with a large radius to make equation 18 deliver “true” amplitudes in images. This is obviously not the case, so some amplitude artifacts can still arise in the elastic images.

Basic imaging algorithms based on the separation of P- and S-waves on the recording surface followed by independent P- and S-wave imaging using procedures borrowed from acoustic wave equation imaging algorithms do not take into account the process of P-to-S or S-to-P conversion along reflectors and at scatterers in the subsurface. Thus, the amount of energy that is properly focused by an imaging condition after wavefield extrapolation based on the acoustic wave equation is relatively small, and is limited to wavepaths that do not involve any conversion (Figure 18). Any P- or S-wave seismic energy recorded on the surface that comes from conversions in the subsurface is not focused by such an imaging condition, and hence creates artifacts in the final image.

Instead of separating wavefields into scalar wave modes on the acquisition surface, the imaging condition proposed by Yan and Sava (2008) uses the full vector fields for wavefield reconstruction. Wavefield separation of scalar and vector potentials is performed just before the imaging condition is applied, and thus it involves the crosscorrelation of pure P or S modes from the source and receiver wavefields. This methodology allows for wave-mode conversions in wavefield reconstruction because the elastic wave equation is used to depth-extrapolate the source and receiver wavefields, and the imaging condition focuses not only pure-modes coming from the source and the receiver wavefields but also waves that experienced wave-modes conversion during extrapolation on either the source or receiver side (Figure 19).

The correlation-type representation theorems in equations 17 and 18 share the same advantages discussed for the elastic imaging condition. Indeed, if we consider only the second surface integral in equation 18 and divide it into integrals depending explicitly on P- or S-wave sources we obtain

$$\begin{aligned}
I_{\psi_N \psi_I, \text{full}}(\mathbf{x}_P) &\approx \frac{2}{\rho c_0} \int_0^{+\infty} \int_{\partial V} G_{\psi_I \psi_0}^{S*}(\mathbf{x}_P, \mathbf{x}) G_{\psi_N \psi_0}^0(\mathbf{x}_P, \mathbf{x}) dx^2 d\omega \\
&+ \frac{2}{\rho c_k} \int_0^{+\infty} \int_{\partial V} G_{\psi_I \psi_k}^{S*}(\mathbf{x}_P, \mathbf{x}) G_{\psi_N \psi_k}^0(\mathbf{x}_P, \mathbf{x}) dx^2 d\omega. \quad (19)
\end{aligned}$$

Monopole sources of P-wave energy are always available in standard industrial marine seismic acquisition systems. However, it is far more difficult to create dipole sources of P-wave energy and inject significant S-wave energy into the ground economically. If we therefore also neglect the S-wave source term, we obtain

$$\begin{aligned}
I_{\psi_N \psi_I}(\mathbf{x}_P) &\approx \frac{2}{\rho c_0} \int_0^{+\infty} \int_{\partial V} G_{\psi_N \psi_0}^0(\mathbf{x}_P, \mathbf{x}) G_{\psi_I \psi_0}^{S*}(\mathbf{x}_P, \mathbf{x}) dx^2 d\omega. \quad (20)
\end{aligned}$$

This is exactly the imaging condition proposed by Yan and Sava (2008), apart from the $2/\rho c_0$ scaling. It shows that the image is created

by crosscorrelating the source wavefield $G_{\psi_r\psi_0}^0(\mathbf{x}_P, \mathbf{x})$, depth-extrapolated by solving numerically the elastic wave equation using as source the same source used during the physical experiment, and the receiver wavefields $G_{\psi_r\psi_0}^S(\mathbf{x}_P, \mathbf{x})$, depth-extrapolated by solving numerically a boundary-value problem for the elastic wave equation where the BC consists of the wavefield recorded on the earth's surface. Only after wavefield reconstruction, the wavefields are separated into scalar and vector potentials and the imaging condition is applied.

Thus, the imaging condition of Yan and Sava (2008) is shown to be a heuristic approximation to the exact, GF-based imaging conditions offered by equations 17 and 18. To summarize, this approximation is obtained by assuming the medium to be homogeneous, isotropic, and unperturbed at and outside of ∂V , by neglecting the crosscorrelation of reference and scattered fields in the first surface integral and the crosscorrelation of scattered fields in the third surface integral, by discarding S-wave sources, by approximating dipole P-wave sources with monopole sources, and by identifying divergence and curl as near-field P- and S-waves, respectively.

Example 3: Elastic imaging of a square

A simple synthetic example is proposed here to compare our new imaging conditions to that of Yan and Sava (2008). An isotropic homogenous medium is used as the background medium, and a high-velocity square that contains a point scatterer at its center is embedded in the reference medium as the perturbation to be imaged (Figure 20). The P-wave velocity of the background medium is $V_P = 1.5$ km/s, the square represents a positive perturbation of $\Delta V_P = 1.3$ km/s, and the point scatterer perturbation S represents a negative perturbation of $\Delta V_P = -1.2$ km/s with respect to the latter. The S-wave velocity is a scaled version of the P-wave velocity, with $V_P/V_S = 2$. P-wave sources are distributed along a circular boundary with radius $r = 0.4$ km to illuminate the target.

The images to be compared are obtained by applying the IC in equation 20 and the IC in equation 18 where S-wave sources are neglected. The Green's functions G^0 and G^S are computed using a staggered-grid, 2D elastic finite-difference algorithm (Virieux, 1986). Here, the receiver wavefield (G^S) is directly modeled rather than obtained by wavefield extrapolation, hence it represents the exact, noiseless scattering response. This removes adverse effects due to a limited receiver geometry on the surface, allowing the two imaging conditions to be compared without additional confounding sources of error. Note that, because only P-wave sources are used, the S-wave component of the source wavefield G^0 is always zero. Hence, we compare the images produced by crosscorrelating the P-wave components of the source wavefield with the P- and S-wave components of the receiver wavefield (I_{PP}, I_{PS}). We interpret the additional contribution of the interaction between scattered wavefields and we analyze the effect of illumination on these images by considering complete

illumination (all sources active) and partial illumination (only top sources active) — see Figure 20.

Complete illumination

In the ideal imaging experiment, the nonlinear imaging condition allows the perturbation to be imaged exactly: Scattering objects are constructed at correct locations with correct amplitudes. A first comparison between the images describing the PP “reflectivity” Green's function (Figure 21a and 21c) shows how the nonlinear imaging condition improves the images obtained from the heuristic imaging condition. The heuristic image (Figure 21a) in fact recovers only the square object; strong “transmission artifacts” (i.e., artifacts due to interactions between the reference wavefield and forward-scattered waves that traverse the square object, see Fleury and Vasconcelos, 2012) contaminate the image preventing a clear definition of its shape. The nonlinear imaging condition (Figure 21c) properly maps the square with the point scatterer at its center and artifacts are significantly reduced.

The heuristic image describing the PS “reflectivity” Green's function (Figure 21b) outlines the edges of the square with a polarity change between left and right sides (most obvious on the horizontal edges of the square). More strikingly, the nonlinear interaction between converted scattered waves (i.e., third integral in equation 18) perfectly matches the contributions of linear interactions between reference and scattered waves (i.e., first and second integrals in equation 18) and results in a final image that is almost

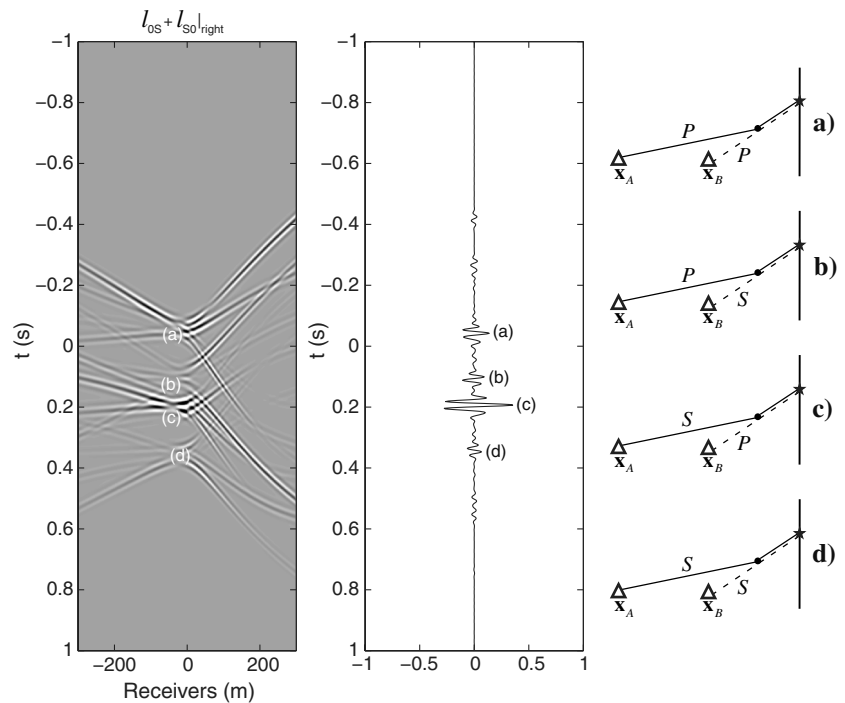


Figure 15. Integrand and stationary points in the crosscorrelation of reference and perturbed wavefields ($I_{OS} + I_{SO}$) that contribute to the generation of nonphysical events in Figure 13. They have a traveltime equal to the difference of (a) P-waves traveling from \mathbf{x}_A to the scatterer and from the scatterer to \mathbf{x}_B , (b) P-waves traveling from \mathbf{x}_A to the scatterer and S-waves traveling from the scatterer to \mathbf{x}_B , (c) S-waves traveling from \mathbf{x}_A to the scatterer and P-waves traveling from the scatterer to \mathbf{x}_B , and (d) S-waves traveling from \mathbf{x}_A to the scatterer and from the scatterer to \mathbf{x}_B .

perfectly null (Figure 21d), with the exception of some weak artifacts around the corners of the square. This result is consistent with the interferometric definition of the imaging condition in equation 18: I_{PS} is the zero time-lag and zero space-lag S-wave response due to a P-wave source. The impossibility to create a conversion from a zero-offset experiment explains why the image is completely null (when the estimate of the total source power loss is accurate at every point thanks to having complete illumination, in contrast to results below).

Partial illumination

We now use an experimental geometry that is closer to real seismic exploration where sources are located only on the earth's surface (i.e., one-sided illumination). The impact of such partial illumination is analyzed by using only the top sources (closed stars in Figure 20) to image the target. The uneven illumination produces

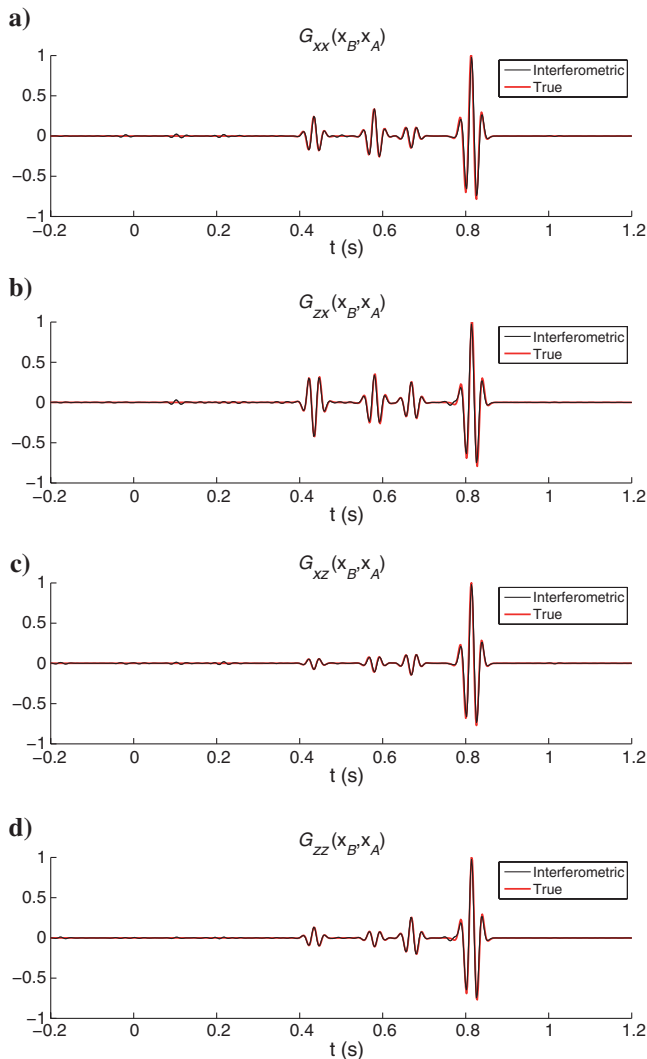


Figure 16. Particle velocity Green's tensor reconstructions with the full interferometric integrals in equation 9 (black line) compared to the true scattered Green's tensor components (red line): (a) $G_{xx}^S(\mathbf{x}_B, \mathbf{x}_A)$, (b) $G_{zx}^S(\mathbf{x}_B, \mathbf{x}_A)$, (c) $G_{xz}^S(\mathbf{x}_B, \mathbf{x}_A)$, (d) $G_{zz}^S(\mathbf{x}_B, \mathbf{x}_A)$.

artifacts on both sides of and below the square for the heuristic PP image (Figure 22a). Although this breaks the power conservation that we use for the nonlinear imaging condition, the nonlinear image is still more accurate and the additional contribution of the interaction between scattered wavefields partially removes the artifacts (especially those on both sides of the square), and also identifies the point scatterer at its center (Figure 22c). Elastic imaging of PP waves thus shows a behavior similar to the acoustic case, even though we conjecture that now the nonlinear contribution focuses not only energy from single-mode multiply scattered waves but also P-wave energy from every kind of converted modes that have been multiply scattered. A more detailed analysis of nonlinear scattering-based purely acoustic imaging can be found in (Fleury and Vasconcelos, 2012).

Imaging of PS-converted waves with an uneven illumination creates images (Figure 22b and 22d) with features that resemble other examples of elastic imaging presented in previous literature (e.g.,

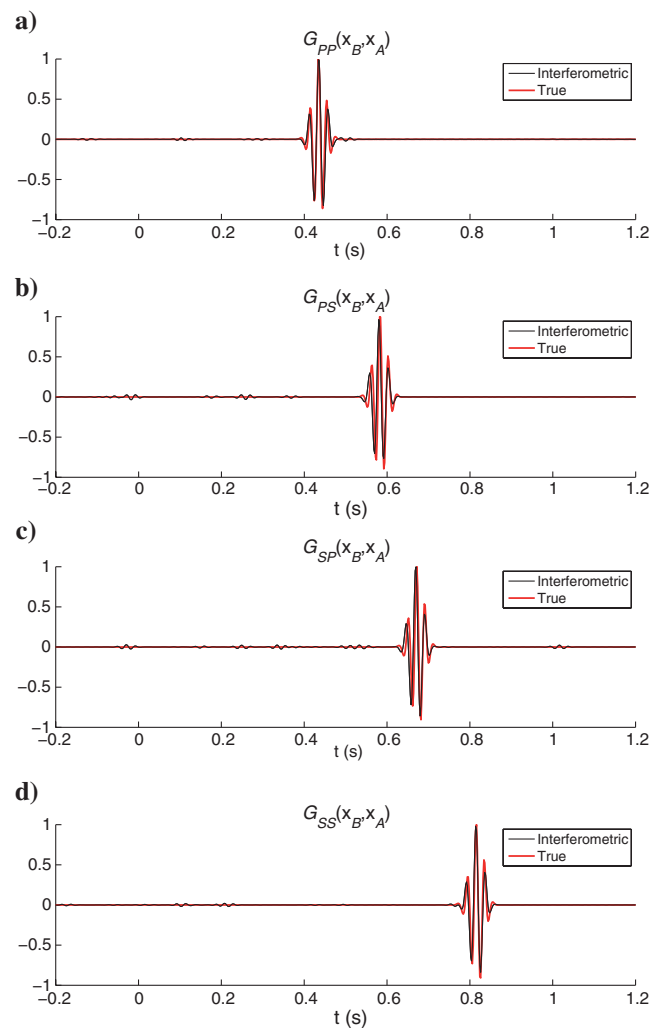


Figure 17. P- or S-wave scattered Green's functions due to P- or S-wave sources, reconstructed with the full interferometric integrals in equation 13 (black line) compared to the true scattered Green's functions (red line): (a) $G_{PP}^S(\mathbf{x}_B, \mathbf{x}_A)$, (b) $G_{PS}^S(\mathbf{x}_B, \mathbf{x}_A)$, (c) $G_{SP}^S(\mathbf{x}_B, \mathbf{x}_A)$, (d) $G_{SS}^S(\mathbf{x}_B, \mathbf{x}_A)$.

Denli and Huang, 2008; Lu et al., 2010). Other than transmission artifacts, present also in the PP images and significantly attenuated by the application of a nonlinear imaging condition (Figure 22d), polarity reversals are evident. They are caused by the different polarizations of converted S-waves with respect to the incident P-wave. Therefore, the sign of the reflection coefficient of a converted PS wave is a function of the P-wave incidence angle (Balch and Erdemir, 1994). Thus, when PS images with flipped polarities are stacked over all the shots, destructive interference occurs and degrades the migration results. This explains how the PS image stacks to exactly zero almost everywhere in Figure 21d; hence the image produced in Figure 22d only shows the structure at all because of the partial illumination. Thus, we observe that although the nonlinear imaging condition provides artifact reduction and illumination compensation for PP and PS images, it does not directly handle the polarity reversal occurring in PS images as is done in other imaging studies. So, to obtain an image using only PS data, further processing could be required before stacking over all the shots to avoid destructive interference as discussed in the next section.

DISCUSSION

Multiply scattered and converted waves can be extremely sensitive to the properties of the medium through which they travel (Gret et al., 2006; Snieder, 2006). They illuminate targets from a wider variety of directions than do primaries, and may be strongly affected by perturbations or errors in average velocity estimates because they have longer path lengths through the medium compared to primaries. This suggests that these waves could usefully be treated as signal rather than noise in imaging. Because multiply scattered waveforms are nonlinearly related to the scattering perturbations in a medium, nonlinear imaging methods are required to properly map their energy into models of subsurface scatterers.

Traditionally, a seismic image is obtained after three stages of processing: First, the smoothly varying part of the earth’s velocity model (i.e., changes in properties over long length scales compared to the wavelength) is estimated by velocity analysis (Taner and Koehler, 1969; Neidell and Taner, 1971). Second, the initial velocity estimates are refined by travelt ime tomography (Bishop, 1985; Stork, 1992) and/or waveform tomography (Pratt, 1999). Third, multiple-free seismic data are projected through the velocity model in an implementation of linearized imaging (i.e., migration). Discontinuities (i.e., changes in properties that occur over short length scales compared to the wavelength) are mapped only using linear interactions between the model and multiple-free data in this third stage. Nonlinear, scattering-based elastic imaging as presented herein can therefore be seen as a fourth stage of imaging, which does not currently exist in standard practice. It requires an a priori estimate of discontinuities, and it promises to “sharpen” images obtained after the usual three stages of imaging.

We have shown that the correlation-type representation theorem for perturbed elastic media with particle-displacement (or P- and S-wave) sources and receivers, used to-date in seismic interferometry for constructing elastic scattered waves via crosscorrelations of observed wavefields for different types of media, can also be used to formulate new nonlinear elastic imaging methods.

A first theorem derived above constructs any combination of P and S scattered waves propagating between two receiver locations, using multicomponent recordings for body-force density sources in

every direction (so-called “9C data”). In land acquisition, only the most advanced multicomponent seismic acquisition systems give a total of nine components for analysis, and for such data this new, exact expression for the reconstruction of full-wavefield P- and S-wave scattered fields can be used for data analysis and imaging. On the other hand, common seismic systems use only vertical vibrators and multicomponent receivers: In these cases, some terms within the reciprocity theorem must be discarded and only an approximate reconstruction can be accomplished. In addition, sources and receivers are usually constrained to the upper part of the bounding surface assumed in these theorems, leading to further approximations in their application. This should not be regarded as a weakness in the theory: On the contrary, the availability of this

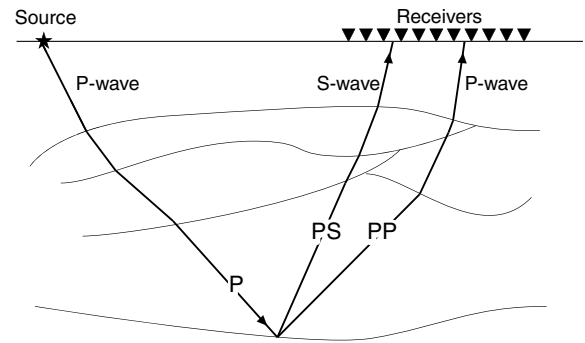


Figure 18. A sketch depicting conventional imaging methods for multicomponent data that separate wave modes on the surface and then depth-extrapolate by solving the acoustic wave equation. The imaging condition focuses energy coming only from the crosscorrelation of pure-wave modes that do not experience any conversion on the wavepath along either source or receiver sides of the main reflection/conversion event. In a marine environment, where the source wavefield can only be a P-wave, crosscorrelation between the source P-wave and the receiver P-wave gives the PP reflectivity function, and crosscorrelation between the source P-wave and the receiver S-wave gives the PS reflectivity function.

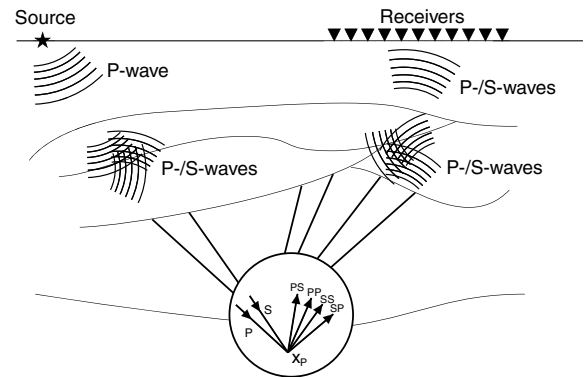


Figure 19. A sketch depicting the full-wavefield imaging condition 17, where the wavefields are depth-extrapolated by solving the elastic wave equation. The imaging condition focuses more energy than that focused by the migration procedures that image P- and S-waves independently (Figure 18) because every kind of reflection and conversion in the subsurface is taken into account during the wavefield extrapolation procedure.

Downloaded 05/02/13 to 129.215.4.143. Redistribution subject to SEG license or copyright; see Terms of Use at http://library.seg.org/

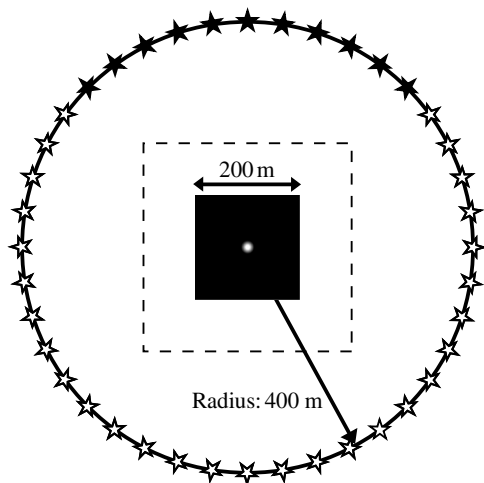


Figure 20. Geometry used for the imaging example. Images were created inside the dashed lines using a circular boundary of 40 P-wave sources. The sides and bottom sources (open stars) are active when the illumination is complete, and inactive when the illumination is partial, whereas the top sources (solid stars) are always active. The P-wave velocity of the background medium is $V_P = 1.5$ km/s, the square represents a positive perturbation of $\Delta V_P = 1.3$ km/s, and the point scatterer S represents a negative perturbation of $\Delta V_P = -1.2$ km/s with respect to the latter. The S-wave velocity is a scaled version of the P-wave velocity, with $V_P/V_S = 2$. A low-velocity point scatterer is located at the center of the square.

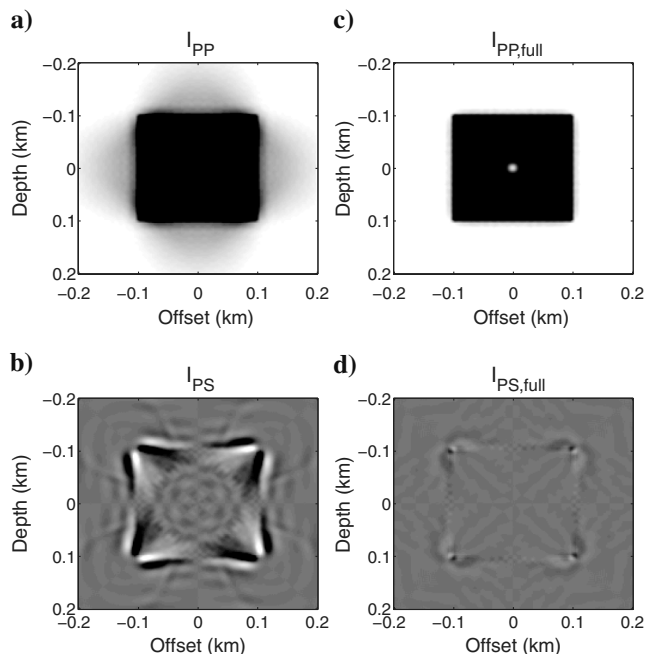


Figure 21. PP and PS images with complete illumination produced using a heuristically derived imaging condition in equation 20 that crosscorrelates P- and S-wave potentials in the subsurface after a full-wavefield extrapolation (Yan and Sava, 2008) on the left and our nonlinear imaging condition equation 18 on the right. Images (a) and (c) are I_{PP} , whereas (b) and (d) are I_{PS} , where $I_{\psi_N \psi_I} = G_{\psi_I \psi_N}^S(\mathbf{x}_P)$. Acquisition geometry with complete illumination is shown in Figure 20 using all sources.

theory means that further studies and synthetic examples will help us to understand the effective contribution coming from the available data types, to test the potential improvements due to future new data types, and to be more aware of the errors that we should expect in the reconstructed Green's function due to the approximations that are necessarily employed.

Using reciprocity relations between only P- and S-wave Green's states, an alternative version of the representation theorem is proposed which is suitable for marine applications using ocean bottom systems. Because waves travel upward and downward at the source boundary (i.e., the medium is not homogenous outside of ∂V as assumed in the P- and S-wave versions of the theory), the estimated scattered wavefield is only an approximated version of the true elastic response between two receivers at positions \mathbf{x}_A and \mathbf{x}_B along the seabed if the monopole approximation is used on the source side. This limitation can be overcome either by using source-side deghosting techniques, or by using the nonapproximated theory with monopoles and dipoles sources (Robertsson et al., 2012).

Similar expressions for full wavefields have been proposed by Halliday et al. (2012), developed using source-receiver interferometry (Curtis and Halliday, 2010) as a basis. They show how this form of interferometry can provide a generalized version of the PP + PS = SS method introduced by Grechka and Tsvankin (2002). Combining our equations 13 and 15 with the theory of source-receiver interferometry could, for example, allow one to identify an expression that reconstructs the scattered SS response from PP and PS recordings. This again illustrates the value of having so comprehensive a theoretical understanding of potentially useful and applicable methods.

Elastic imaging is one of the main challenges in industrial geophysics, and from existing literature and practice it is still not clear which is the best way to use vector displacements or vector potentials to obtain an accurate image of the subsurface. An explicit relation between the recent practice of elastic wavefield-based seismic imaging and the theory of representation theorems has been derived in this paper. Because representation theorems are exact expressions for wavefields, we conjecture that our equations 17 and 18 can guide future intuition to better combine scalar and vectorial potentials, obtained from different body-force density sources or P- and S-wave sources and separated in the subsurface. Thus, we identify full-wavefield imaging conditions that in the case of full illumination from all directions produce true-amplitude images, accounting not only for every kind of nonlinear effect (e.g., multiples, and nonlinear scattering described by optical theorems — Snieder et al., 2008; Halliday and Curtis, 2009; Margerin and Sato, 2011) but also for conversions occurring at different interfaces and diffractors. This is certainly true when an exact velocity model is used to obtain an estimate of scattering terms present in nonlinear imaging conditions; however, because the accuracy of these terms is affected when the velocity model is in error (short length-scale discontinuities will be mispositioned), further research into the sensitivity of imaging using multiple events in seismic data with respect to errors in the model estimate is necessary in future.

A simple synthetic example showed how the contribution coming from a previously published heuristically derived imaging condition (crosscorrelation between direct and scattered waves) and the nonlinear contribution from the autocorrelation of scattered waves are complementary. Combined together they create an image of the

target that is consistent with the definition of the zero-time, scattered-wave response generated by a zero-offset pseudo experiment ($G_{\psi_1\psi_N}^S(\mathbf{x}_P, \mathbf{x}_P, \tau = 0)$). Under ideal illumination (e.g., Figure 21), the nonlinear contribution for PP imaging removes artifacts otherwise observed around the perturbation and improves the definition of its edges. This term assumes more significance in PS imaging because it perfectly matches the contributions of linear interactions between reference and scattered waves and results in a final image that is perfectly null. Our definition of a reciprocity-based IC can explain this result, overcoming the intrinsic limitations of heuristically based ICs. The image is null because no conversion arises from a zero-offset experiment.

However, a zero time-lag and zero space-lag crosscorrelation IC creates a nonzero image for converted waves when evaluated using one-sided illumination. This fact has previously prevented a full understanding of the processes involved in converted wave imaging. Many attempts have been made to image reflectors and diffractors in the subsurface using converted-wave PS energy, and to mitigate the “natural” destructive interference that occurs while stacking over all shots (see Yan and Sava [2008] and references therein). The fact that converted S-waves have different polarizations based on the P-wave incidence angle has led authors to preprocess (reverse) some converted wave polarizations before stacking. As a rule of thumb, we can assume that the polarity change occurs between either side of zero offset, and can be corrected by multiplying by -1 on one side of the shot position while keeping the other side unchanged (e.g., Figure 23). A more sophisticated procedure proposed by Balch and Erdemir (1994) corrects for this reversal in complex background velocity models by estimating the P-wave incidence angle for every image point using a ray approximation, and demonstrated its feasibility in a cross-borehole experiment. Denli and Huang (2008) defined a wavefield-separation imaging condition based on the separation of wavefields with respect to a given direction using f - k filters after the elastic wavefields are downward propagated. Rosales et al. (2008) and Lu et al. (2010) suggested an approach in which the angle-domain common-image gathers (Sava and Fomel, 2003) are computed at every image point and the polarity is corrected in the angle domain before stacking. Finally, Du et al. (2012) introduced a sign factor to represent the polarity distribution of the S-wave component; this sign factor is computed using the energy flux density vector.

From our results above, we can conclude that if the zero-time scattered-wave response generated by zero-offset pseudoexperiments is a good candidate to be used as an imaging condition for single-mode elastic waves, it may not be the best condition for imaging of converted-mode elastic waves. Every attempt to reduce or remove the destructive summation can now be seen as an attempt to obtain an image that does not resemble the zero-time, scattered-wave response generated by zero-offset pseudoexperiments. We conjecture that a more appropriate context for imaging of converted waves is represented by extended images (Sava and Vasconcelos, 2011). The evaluation of an imaging condition at non-zero subsurface offset could effectively extract the energy coming from the conversion process at any discontinuity in the subsurface. Further studies will be carried out in this direction.

Moreover, an IC that describes the received scattered P- or S-wave due to a colocated P- or S-wave source and receiver contradicts the fact that when using physical point sources the P- and S-waves can be defined only in the far-field. Although the applica-

tion of divergence and curl to particle displacement recordings is still valid, the result of such an IC should be interpreted as a near-field projection of the far-field P- and S-waves crosscorrelated at the image point.

For these reasons, only an elastic imaging condition based on the full elastic wavefield can truly express the local interaction in the subsurface, as if real unidirectional point force sources and particle displacement (or velocity) receivers were colocated at each image point. Such an IC can be obtained by writing equation 9 with $\mathbf{x}_P = \mathbf{x}_A = \mathbf{x}_B$ and integrating over frequencies (ω)

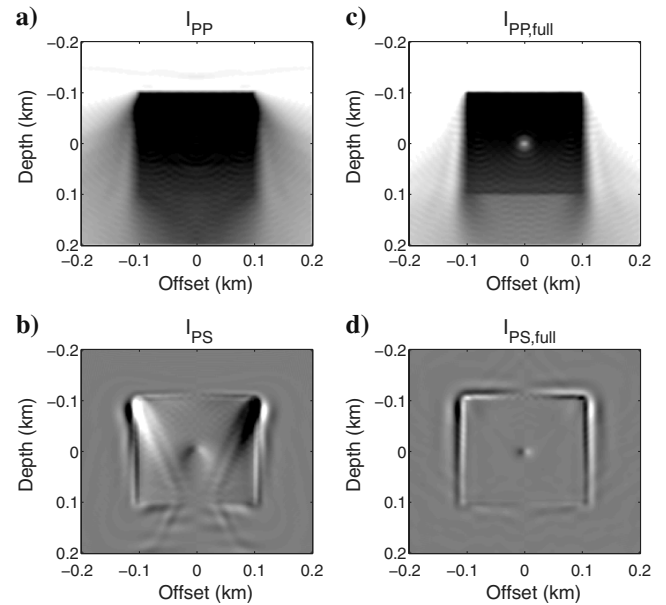


Figure 22. PP and PS images with only partial illumination produced using the heuristically derived imaging condition of Yan and Sava (2008) in equation 20 on the left, and our nonlinear imaging condition equation 18 on the right. Images (a) and (c) are I_{PP} , whereas (b) and (d) are I_{PS} , where $I_{\psi_N\psi_1} = G_{\psi_1\psi_N}^S(\mathbf{x}_P)$. Acquisition-geometry with partial illumination is shown in Figure 20 using only top sources.

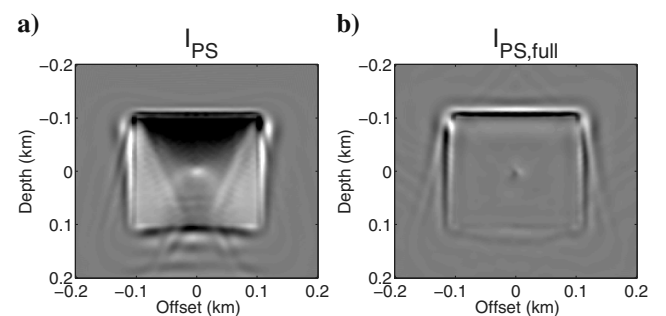


Figure 23. PS images with only the partial illumination in Figure 22 when polarity correction is applied before stacking for (a) linear and (b) nonlinear imaging. Nonlinear terms still contribute to reduce artifacts around the interfaces, and to sharpen up the entire image.

$$\begin{aligned}
I_{ni,full}(\mathbf{x}_P) &= 2 \int_0^{+\infty} \text{Re}\{G_{in}^S(\mathbf{x}_P)\}d\omega \\
&= \int_0^{+\infty} \frac{1}{j\omega} \int_{\partial V} \{G_{im}^{0*}(\mathbf{x}_P, \mathbf{x})n_j c_{mjkl}^0 \partial_k G_{nl}^S(\mathbf{x}_P, \mathbf{x}) \\
&\quad - G_{nm}^S(\mathbf{x}_P, \mathbf{x})n_j c_{mjkl}^0 \partial_k G_{il}^{0*}(\mathbf{x}_P, \mathbf{x})\}d\mathbf{x}^2 d\omega \\
&\quad + \int_0^{+\infty} \frac{1}{j\omega} \int_{\partial V} \{G_{im}^{S*}(\mathbf{x}_P, \mathbf{x})n_j c_{mjkl}^0 \partial_k G_{nl}^0(\mathbf{x}_P, \mathbf{x}) \\
&\quad - G_{nm}^0(\mathbf{x}_P, \mathbf{x})n_j c_{mjkl}^0 \partial_k G_{il}^{S*}(\mathbf{x}_P, \mathbf{x})\}d\mathbf{x}^2 d\omega \\
&\quad + \int_0^{+\infty} \frac{1}{j\omega} \int_{\partial V} \{G_{im}^{S*}(\mathbf{x}_P, \mathbf{x})n_j c_{mjkl}^0 \partial_k G_{nl}^S(\mathbf{x}_P, \mathbf{x}) \\
&\quad - G_{nm}^S(\mathbf{x}_P, \mathbf{x})n_j c_{mjkl}^0 \partial_k G_{il}^{S*}(\mathbf{x}_P, \mathbf{x})\}d\mathbf{x}^2 d\omega. \quad (21)
\end{aligned}$$

This imaging condition will be the subject of future investigation.

CONCLUSION

In this paper, a correlation-type representation theorem for perturbed elastic media is derived. The contributions of various surface integrals are explained using two simple acoustic examples through a stationary-phase analysis. The interior workings of the elastic scattering representation theorem is illustrated using an elastic isotropic example. We then derive alternative versions of these scattered-wave theorems for the cases where P- and S-wave sources and/or receivers are available. We suggest potential applications of these formulae in land and marine seismic acquisition.

Starting from a representation theorem with P- or S-wave receivers, we have proposed two nonlinear, true-amplitude imaging conditions. These account also for multiply scattered waves and every kind of wavefield conversion in the subsurface, facilitating a fourth stage of nonlinear elastic imaging, when an estimate of the velocity model with short-scale discontinuities has already been estimated by the usual three stages of velocity analysis, waveform tomography, and linear migration. We have also shown that the imaging condition with P- or S-wave sources on the earth's surface can be turned into a previously published elastic imaging condition that crosscorrelates pure modes separated in the subsurface after a full-wavefield extrapolation. However, this is only possible if our imaging conditions are severely approximated. Thus, our new full wavefield ICs are shown to be theoretically exact versions of the previous heuristically derived ICs. This result creates an explicit link between theory of seismic interferometry and elastic seismic imaging, and sheds new light on how to create true-amplitude elastic images.

ACKNOWLEDGMENTS

The authors thank Ivan Vasconcelos (Schlumberger Gould Research) and Giovanni Angelo Meles (University of Edinburgh) for insightful discussions and helpful suggestions. We are also grateful to the associate Editor Deyan Draganov, Kees Wapenaar, and two other anonymous reviewers for their invaluable comments that helped to improve the manuscript. We thank the Edinburgh Interferometry Project (EIP) sponsors, ConocoPhillips, Schlumberger Cambridge Research, Statoil, and Total for supporting this research and granting us permission to publish it.

REFERENCES

- Aki, K., and P. G. Richards, 1980, Quantitative seismology: W. H. Freeman & Co.
- Balch, A., and C. Erdemir, 1994, Sign-change correction for prestack migration of *P-S* converted wave reflections: *Geophysical Prospecting*, **42**, 637–663, doi: [10.1111/gpr.1994.42.issue-6](https://doi.org/10.1111/gpr.1994.42.issue-6).
- Bishop, T. N., 1985, Tomographic determination of velocity and depth in laterally varying media: *Geophysics*, **50**, 903–923, doi: [10.1190/1.1441970](https://doi.org/10.1190/1.1441970).
- Brossier, R., S. Operto, and J. Virieux, 2009, Seismic imaging of complex onshore structures by 2D elastic frequency-domain full-waveform inversion: *Geophysics*, **74**, no. 6, WCC105–WCC118, doi: [10.1190/1.3215771](https://doi.org/10.1190/1.3215771).
- Claerbout, J. F., 1971, Toward a unified theory of reflector mapping: *Geophysics*, **36**, 467–481, doi: [10.1190/1.1440185](https://doi.org/10.1190/1.1440185).
- Claerbout, J. F., 1985, *Imaging the earth's interior*: Blackwell Scientific Publications, Inc.
- Curtis, A., 2009, Source-receiver seismic interferometry: 79th Annual International Meeting, SEG, Expanded Abstracts, 3655–3658.
- Curtis, A., Y. Behr, E. Entwistle, E. Galetti, J. Townend, and S. Bannister, 2012, The benefit of hindsight in observational science: Retrospective seismological observations: *Earth and Planetary Science Letters*, **345–348**, 212–220, doi: [10.1016/j.epsl.2012.06.008](https://doi.org/10.1016/j.epsl.2012.06.008).
- Curtis, A., P. Gerstoft, H. Sato, R. Snieder, and K. Wapenaar, 2006, Seismic interferometry — turning noise into signal: *The Leading Edge*, **25**, 1082–1092, doi: [10.1190/1.2349814](https://doi.org/10.1190/1.2349814).
- Curtis, A., and D. Halliday, 2010, Source-receiver wave field interferometry: *Physical Review*, **81**.
- Curtis, A., H. Nicolson, D. Halliday, J. Trampert, and B. Baptie, 2009, Virtual seismometers in the subsurface of the earth from seismic interferometry: *Nature Geoscience*, 700–704, doi: [10.1038/ngeo615](https://doi.org/10.1038/ngeo615).
- Denli, H., and L. Huang, 2008, Elastic-wave reverse-time migration with a wavefield separation imaging condition: 78th Annual International Meeting, SEG, Expanded Abstracts, 2346–2350.
- Douma, H., I. Vasconcelos, and R. Snieder, 2011, The reciprocity theorem for the scattered field is the progenitor of the generalized optical theorems: *Journal of the Acoustical Society of America*, **129**, 2765–2771, doi: [10.1121/1.3569728](https://doi.org/10.1121/1.3569728).
- Du, Q., Y. Zhu, and J. Ba, 2012, Polarity reversal correction for elastic reverse time migration: *Geophysics*, **77**, no. 2, S31–S41, doi: [10.1190/geo2011-0348.1](https://doi.org/10.1190/geo2011-0348.1).
- FlEURY, C., and I. Vasconcelos, 2012, Imaging condition for nonlinear scattering-based imaging: Estimate of power loss in scattering: *Geophysics*, **77**, no. 1, S1–S18, doi: [10.1190/geo2011-0135.1](https://doi.org/10.1190/geo2011-0135.1).
- Gaiser, J. E., and I. Vasconcelos, 2010, Elastic interferometry for ocean bottom cable data: Theory and examples: *Geophysical Prospecting*, **58**, 347–360, doi: [10.1111/\(ISSN\)1365-2478](https://doi.org/10.1111/(ISSN)1365-2478).
- Galetti, E., and A. Curtis, 2012, Generalised receiver functions and seismic interferometry: *Tectonophysics*, **532–535**, 1–26.
- Grechka, V., and I. Tsvankin, 2002, PP + PP = SS: *Geophysics*, **67**, 1961–1971, doi: [10.1190/1.1527096](https://doi.org/10.1190/1.1527096).
- Gret, A., R. Snieder, and J. Scales, 2006, Time-lapse monitoring of rocks properties with coda wave interferometry: *Journal of Geophysical Research*, **111**, B03305, doi: [10.1029/2004JB003354](https://doi.org/10.1029/2004JB003354).
- Halliday, D., and A. Curtis, 2009, Generalized optical theorem for surface waves and layered media: *Physical Review E*, **79**, 056603, doi: [10.1103/PhysRevE.79.056603](https://doi.org/10.1103/PhysRevE.79.056603).
- Halliday, D., and A. Curtis, 2010, An interferometric theory of source-receiver scattering and imaging: *Geophysics*, **75**, no. 6, SA95–SA103, doi: [10.1190/1.3486453](https://doi.org/10.1190/1.3486453).
- Halliday, D., A. Curtis, and K. Wapenaar, 2012, Generalized PP + PS = SS from seismic interferometry: *Geophysical Journal International*, **189**, 1015–1024, doi: [10.1111/gji.2012.189.issue-2](https://doi.org/10.1111/gji.2012.189.issue-2).
- Hong, T.-K., and W. Menke, 2006, Tomographic investigation of the wear along the San Jacinto fault, southern California: *Physics of the Earth and Planetary Interiors*, **155**, 236–248, doi: [10.1016/j.pepi.2005.12.005](https://doi.org/10.1016/j.pepi.2005.12.005).
- Lu, L., Z. Ding, R. S. Zeng, and Z. He, 2011, Retrieval of Green's function and generalized optical theorem for scattering of complete dyadic fields: *Journal of the Acoustical Society of America*, **129**, 1935–1944, doi: [10.1121/1.3553224](https://doi.org/10.1121/1.3553224).
- Lu, R., J. Yan, J. E. Anderson, and T. Dickens, 2010, Elastic RTM: Anisotropic wave-mode separation and converted-wave polarization correction: 80th Annual International Meeting, SEG, Expanded Abstracts, 3171–3175.
- Margerin, L., and H. Sato, 2011, Generalized optical theorems for the reconstruction of Green's function of an inhomogeneous elastic medium: *Journal of the Acoustical Society of America*, **130**, 3674–3690, doi: [10.1121/1.3652856](https://doi.org/10.1121/1.3652856).
- Mora, P., 1987, Nonlinear two-dimensional elastic inversion of multi offset seismic data: *Geophysics*, **52**, 1211–1228, doi: [10.1190/1.1442384](https://doi.org/10.1190/1.1442384).

- Neidell, N., and M. Taner, 1971, Semblance and other coherency measures for multichannel data: *Geophysics*, **36**, 482–497, doi: [10.1190/1.1440186](https://doi.org/10.1190/1.1440186).
- Oristaglio, M. L., 1989, An inverse-scattering formula that uses all the data: *Inverse Problems*, **5**, 1097–1105, doi: [10.1088/0266-5611/5/6/015](https://doi.org/10.1088/0266-5611/5/6/015).
- Plessix, R., 2006, A review of the adjoint-state method for computing the gradient of a functional with geophysical applications: *Geophysical Journal International*, **167**, 495–503, doi: [10.1111/gji.2006.167.issue-2](https://doi.org/10.1111/gji.2006.167.issue-2).
- Pratt, R., 1999, Seismic waveform inversion in the frequency domain, part 1: Theory and verification in a physical scale model: *Geophysics*, **64**, 888–901, doi: [10.1190/1.1444597](https://doi.org/10.1190/1.1444597).
- Robertsson, J. O. A., J. O. Blanch, and W. W. Symes, 1994, Viscoelastic finite-difference modeling: *Geophysics*, **59**, 1444–1456, doi: [10.1190/1.1443701](https://doi.org/10.1190/1.1443701).
- Robertsson, J. O. A., D. Halliday, D.-J. van Manen, I. Vasconcelos, R. Laws, K. Ozdemir, and H. Gronaas, 2012, Full-wavefield, towed-marine seismic acquisition and applications: Presented at the 74th Annual International Conference and Exhibition, EAGE.
- Rosales, D. A., S. Fomel, B. L. Biondi, and P. Sava, 2008, Wave-equation angle-domain common-image gathers for converted waves: *Geophysics*, **73**, no. 1, S17–S26, doi: [10.1190/1.2821193](https://doi.org/10.1190/1.2821193).
- Sava, P., and S. Fomel, 2003, Angle-domain common-image gathers by wavefield continuation methods: *Geophysics*, **68**, 1065–1074, doi: [10.1190/1.1581078](https://doi.org/10.1190/1.1581078).
- Sava, P., and I. Vasconcelos, 2011, Extended imaging condition for wave-equation migration: *Geophysical Prospecting*, **59**, 35–55, doi: [10.1111/gpr.2010.59.issue-1](https://doi.org/10.1111/gpr.2010.59.issue-1).
- Sears, T., S. Singh, and P. Barton, 2008, Elastic full waveform inversion of multi-component OBC seismic data: *Geophysical Prospecting*, **56**, 843–862, doi: [10.1111/gpr.2008.56.issue-6](https://doi.org/10.1111/gpr.2008.56.issue-6).
- Slob, E., D. Draganov, and K. Wapenaar, 2007, Interferometric electromagnetic Green's functions representations using propagation invariants: *Geophysical Journal International*, **169**, 60–80, doi: [10.1111/gji.2007.169.issue-1](https://doi.org/10.1111/gji.2007.169.issue-1).
- Snieder, R., 2002, *Scattering and inverse scattering in pure and applied science*: Academic Press, Inc.
- Snieder, R., 2006, The theory of coda wave interferometry: *Pure and Applied Geophysics*, **163**, 455–473, doi: [10.1007/s00024-005-0026-6](https://doi.org/10.1007/s00024-005-0026-6).
- Snieder, R., K. van Wijk, M. Haney, and R. Calvert, 2008, The cancellation of spurious arrivals in Green's function extraction and the generalized optical theorems: *Physical Review E*, **78**, doi: [10.1103/PhysRevE.78.036606](https://doi.org/10.1103/PhysRevE.78.036606).
- Stork, C., 1992, Reflection tomography in the postmigrated domain: *Geophysics*, **57**, 680–692, doi: [10.1190/1.1443282](https://doi.org/10.1190/1.1443282).
- Taner, M., and F. Koehler, 1969, Velocity spectra, digital computer derivation applications of velocity functions: *Geophysics*, **34**, 859–881, doi: [10.1190/1.1440058](https://doi.org/10.1190/1.1440058).
- Tarantola, A., 1986, A strategy for nonlinear elastic inversion of seismic reflection data: *Geophysics*, **51**, 1893–1903, doi: [10.1190/1.1442046](https://doi.org/10.1190/1.1442046).
- Tromp, J., C. Tape, and Q. Liu, 2005, Seismic tomography, adjoint methods, time reversal and banana-doughnut kernels: *Geophysical Journal International*, **160**, 195–216, doi: [10.1111/gji.2005.160.issue-1](https://doi.org/10.1111/gji.2005.160.issue-1).
- van Manen, D.-J., A. Curtis, and J. O. A. Robertsson, 2006, Interferometric modeling of wave propagation in inhomogeneous elastic media using time reversal and reciprocity: *Geophysics*, **71**, no. 4, SI47–SI60, doi: [10.1190/1.2213218](https://doi.org/10.1190/1.2213218).
- van Manen, D.-J., J. O. A. Robertsson, and A. Curtis, 2005, Modeling of wave propagation in inhomogeneous media: *Physical Review Letters*, **94**, 164301, doi: [10.1103/PhysRevLett.94.164301](https://doi.org/10.1103/PhysRevLett.94.164301).
- Vasconcelos, I., 2008a, Generalized representations of perturbed fields—applications in seismic interferometry and migration: 78th Annual International Meeting, SEG, Expanded Abstracts, 2927–2941.
- Vasconcelos, I., 2011, Source-receiver reverse-time imaging of vector-acoustic seismic data: 81st Annual International Meeting, SEG, Expanded Abstracts, 3184–3189.
- Vasconcelos, I., J. Robertsson, M. Vassallo, and D.-J. van Manen, 2012, Reverse-time imaging of dual-source 4C marine seismic data using primaries, ghosts, and multiples: Presented at the 74th Annual International Conference and Exhibition, EAGE.
- Vasconcelos, I., P. Sava, and H. Douma, 2009a, Wave-equation extended images via image-domain interferometry: 79th Annual International Meeting, SEG, Expanded Abstracts, 2839–2843.
- Vasconcelos, I., P. Sava, and H. Douma, 2010, Nonlinear extended images via image-domain interferometry: *Geophysics*, **75**, no. 6, SA105–SA115, doi: [10.1190/1.3494083](https://doi.org/10.1190/1.3494083).
- Vasconcelos, I., and R. Snieder, 2008a, Interferometry by deconvolution: Part 1 — Theory for acoustic waves and numerical examples: *Geophysics*, **73**, no. 3, S115–S128, doi: [10.1190/1.2904554](https://doi.org/10.1190/1.2904554).
- Vasconcelos, I., and R. Snieder, 2008b, Interferometry by deconvolution: Part 2 — Theory for elastic waves and application to drill-bit seismic imaging: *Geophysics*, **73**, no. 3, S129–S141, doi: [10.1190/1.2904985](https://doi.org/10.1190/1.2904985).
- Virieux, J., 1986, S-SV wave propagation in heterogeneous media: Velocity-stress finite-difference method: *Geophysics*, **51**, 889–901, doi: [10.1190/1.1442147](https://doi.org/10.1190/1.1442147).
- Wapenaar, C., and G. Haimé, 1990, Elastic extrapolation of seismic P- and S-waves: *Geophysical Prospecting*, **38**, 23–60, doi: [10.1111/gpr.1990.38.issue-1](https://doi.org/10.1111/gpr.1990.38.issue-1).
- Wapenaar, C. P. A., 1996, Inversion versus migration: A new perspective to an old discussion: *Geophysics*, **61**, 804–814, doi: [10.1190/1.1444005](https://doi.org/10.1190/1.1444005).
- Wapenaar, K., 2004, Retrieving the elastodynamic Green's function of an arbitrary inhomogeneous medium by cross correlation: *Physical Review Letters*, **93**, 254301, doi: [10.1103/PhysRevLett.93.254301](https://doi.org/10.1103/PhysRevLett.93.254301).
- Wapenaar, K., D. Draganov, R. Snieder, X. Campman, and A. Verdel, 2010a, Tutorial on seismic interferometry: Part 1 — Basic principles and applications: *Geophysics*, **75**, no. 5, 75A195–75A209, doi: [10.1190/1.3457445](https://doi.org/10.1190/1.3457445).
- Wapenaar, K., and J. Fokkema, 2006, Green's function representations for seismic interferometry: *Geophysics*, **71**, no. 4, SI33–SI46, doi: [10.1190/1.2213955](https://doi.org/10.1190/1.2213955).
- Wapenaar, K., E. Slob, and R. Snieder, 2010c, On seismic interferometry, the generalized optical theorem, and the scattering matrix of a point scatterer: *Geophysics*, **75**, no. 3, SA27–SA35, doi: [10.1190/1.3374359](https://doi.org/10.1190/1.3374359).
- Wapenaar, K., E. Slob, R. Snieder, and A. Curtis, 2010b, Tutorial on seismic interferometry: Part 2 — Underlying theory and new advances: *Geophysics*, **75**, no. 5, 75A211–75A227, doi: [10.1190/1.3463440](https://doi.org/10.1190/1.3463440).
- Wu, R. S., and A. Ben-Menahem, 1985, The elastodynamic near field: *Geophysical Journal of the Royal Astronomical Society*, **81**, 609–621, doi: [10.1111/gji.1985.81.issue-3](https://doi.org/10.1111/gji.1985.81.issue-3).
- Yan, J., and P. Sava, 2008, Isotropic angle-domain elastic reverse-time migration: *Geophysics*, **73**, no. 6, S229–S239, doi: [10.1190/1.2981241](https://doi.org/10.1190/1.2981241).
- Yilmaz, O., 1989, *Seismic data processing*: SEG.